

Navigating the complexity of detrital rutile provenance: Methodological insights from the Neotethys Orogen in Anatolia

Megan A. Mueller^{1,2,*}, Alexis Licht^{1,3}, Andreas Möller⁴, Cailey B. Condit¹, Julie C. Fosdick², Faruk Oçakoğlu⁵, Clay Campbell⁶

¹. Department of Earth and Space Sciences, University of Washington, 4000 15th Avenue NE, Seattle, WA 98195, USA

². Department of Earth Sciences, University of Connecticut, 354 Mansfield Road - Unit 1045, Storrs, CT 06269, USA

³. Aix-Marseille Université, CNRS, IRD, INRAE, Collège de France, CEREGE, Technopôle de l'Arbois-Méditerranée, BP80, 13545 Aix-en-Provence, France

⁴. Department of Geology, The University of Kansas, 1414 Naismith Drive, Lawrence, KS 66045, USA

⁵. Department of Geological Engineering, Eskişehir Osmangazi University, Büyükdere, 26040 Eskişehir, Türkiye

⁶. Department of Geosciences, University of Arizona, 1040 E 4th St, Tucson, AZ 85721, USA

* Now at Department of Earth and Planetary Sciences, Jackson School of Geosciences, The University of Texas at Austin, 2305 Speedway Stop C1160, Austin, TX 78712, USA

Correspondence to: Megan Mueller (megan.mueller@jsg.utexas.edu)

Abstract. Sedimentary provenance is a powerful tool for reconstructing convergent margin evolution. Yet single mineral approaches, like detrital zircon, have struggled to track sediment input from mafic and metamorphic sources. Detrital rutile complements detrital zircon datasets by offering a path forward in sedimentary provenance reconstructions where metamorphic terranes are potential source regions. However, U-Pb geochronology in rutile can be difficult due to low uranium concentrations and incorporation of common Pb, and multiple workflows are currently in use. Here, we investigate U-Pb and trace element data reduction, processing, and common Pb correction workflows using new detrital rutile U-Pb geochronology and trace element geochemistry results from the Late Cretaceous to Eocene Central Sakarya and Sarıcakaya Basins in Anatolia. A significant number of analyses were rejected (54%) due to signal intensity limitations, namely low U, low Pb, anomalous signal, and inclusions. We identify this as a universal limitation of large-*n* detrital rutile studies and recommend the systematic reporting of the amount of discarded analysis and the processes for rejection in all studies using detrital rutile U-Pb geochronology. Additionally, we show that (1) the ²⁰⁸Pb and ²⁰⁷Pb common Pb reduction schemes produce similar age distributions and can be used indifferently; (2) The Stacey-Kramers distance is a suitable metric for quantifying U-Pb discordance but a discordance filter is not recommended; (3) Instead, filtering U-Pb data by a power law function based on corrected date uncertainty is appropriate; (4) The exclusion of low uranium concentration rutile biases date distributions and favors pelitic-derived, higher Zr-in-rutile temperature, higher U-Pb concordance grains; (5) Paired U-Pb and trace elements

30 can be used to evaluate potential bias in U-Pb data rejection, which reveals that data rejection does not bias the provenance
31 interpretations; (6) The signature of sediment recycling can be identified through U-Pb dates and Zr-in-rutile temperatures. To
32 better navigate the complexity of detrital rutile datasets and to facilitate the standardization of data reporting approaches, we
33 provide open access code as Jupyter Notebooks for data processing and analysis steps, including common Pb corrections,
34 uncertainty filters, discordance calculations, and trace element analysis.

35 **1 Introduction**

36 Sedimentary provenance analysis is widely used to reconstruct ancient sediment dispersal networks, source-to-sink
37 sediment budgets, sedimentary basin evolution, and to discern links between tectonics, geodynamics, paleogeography, climate,
38 and biologic evolution (Dickinson and Suczek, 1979; Garzanti et al., 2007; Clift et al., 2008; Gehrels, 2014; Blum and Pecha,
39 2014). Compositional provenance methods include sediment petrologic, chemical, and heavy mineral characterizations (e.g.,
40 Gazzi, 1965; Hubert, 1971; Dickinson and Suczek, 1979; Morton, 1985; Garzanti and Andò, 2007). Over the last several
41 decades, the rise of chronometric and geochemical techniques led to the increase in single-mineral approaches. Detrital zircon
42 U-Pb geochronology has become the most widely used technique as zircon is refractory and is abundant in crustal rocks (e.g.,
43 Gehrels, 2014). Further, the age, thermal history, and elemental and isotopic composition of detrital zircons can quantitatively
44 reconstruct both sedimentary provenance and geodynamic, tectonic, and magmatic processes (Carrapa, 2010; Paterson and
45 Ducea, 2015; Tang et al., 2020; Sundell et al., 2022). However, one major limitation is that zircons predominantly form in
46 intermediate to felsic magmas, thus detrital zircon suites generally lack information about mafic igneous and metamorphic
47 processes and sources (Hietpas et al., 2011; Moecher et al., 2011; Gaschnig, 2019). Zircon is present in metamorphic rocks as
48 inclusions in other minerals or as recrystallized-dissolved-reprecipitated rims on zircon cores (Kohn and Kelly, 2017). The
49 outer growth domains of zircons can be targeted with laser ablation ICP-MS depth profiling, or with spot analysis if the rims
50 are thick enough, yet the most commonly used techniques for rapid provenance data acquisition do not routinely analyze zircon
51 rims. Therefore, sedimentary provenance interpretations based on detrital zircon alone are incomplete. For this reason the
52 sedimentary provenance community is increasingly turning to U-Th-Pb and trace elements in phases commonly used in
53 petrochronology, such as detrital rutile (Zack et al., 2004a; Meinhold, 2010; Triebold et al., 2012; Bracciali et al., 2013; Rösel
54 et al., 2014, 2019; O'Sullivan et al., 2016; Odum et al., 2019; Pereira et al., 2020), detrital apatite (Morton and Yaxley, 2007;
55 Chew et al., 2011; Mark et al., 2016; O'Sullivan et al., 2016, 2020), detrital monazite (Hietpas et al., 2010; Moecher et al.,
56 2011; Gaschnig, 2019), and detrital titanite (Guo et al., 2020; Chew et al., 2020), in addition to other isotopic systems in these
57 and other detrital minerals.

58 Detrital rutile is a complementary sedimentary provenance proxy to detrital zircon. Rutile forms in metamafic and
59 metapelitic rocks across a range of P-T conditions, therefore, detrital rutile is especially advantageous when tracking sediment
60 input from greenschist to eclogite or granulite facies sources (e.g., Meinhold, 2010; Zack and Kooijman, 2017). The
61 geochemical composition of rutile can further distinguish between metamorphic protoliths (e.g., Triebold et al., 2007, 2012;

62 Meinhold, 2010). However, rutile U-Pb analysis is challenging due to low U and low radiogenic Pb concentrations and due to
63 the incorporation of initial non-radiogenic Pb. Here, we use a new detrital rutile petrochronology dataset from Anatolia to
64 investigate data reduction, processing and analytical steps in order to support robust provenance interpretations. In a number
65 of studies, analyses have been discarded during U-Pb data reduction due to unacceptable signal intensity (e.g. Bracciali et al.,
66 2013; Rösel et al., 2014, 2019), and we find that discarding analyses is a limitation to large-*n* detrital rutile datasets in the
67 literature and this study. We test the sensitivity of resulting U-Pb date spectra to Pb correction methods, uncertainty and
68 discordance filters, and a low U cutoff threshold. Ultimately, the new dataset demonstrates that detrital rutile captures sediment
69 input from a subduction accretion complex that is poorly resolved in the detrital zircon record. Despite the described
70 limitations, detrital rutile petrochronology can be effectively used to reconstruct sedimentary provenance, deformation,
71 metamorphism, and sediment recycling.

72 **2 Detrital Rutile Provenance**

73 **2.1 Detrital Rutile Synopsis**

74 The advantages of detrital rutile provenance are extensively documented (e.g., Zack et al., 2004a; Meinhold, 2010;
75 Triebold et al., 2012; Bracciali, 2019; Gaschnig, 2019; Pereira et al., 2020; Pereira and Storey, 2023) so we provide only a
76 brief overview here. Rutile is the most common TiO₂ polymorph, a common accessory mineral in metamorphic and igneous
77 rocks (Meinhold, 2010; Zack and Kooijman, 2017), and an abundant heavy mineral in sedimentary rocks (Morton, 1985).
78 Rutile is present across a range of P–T conditions: rutile is generally stable at the surface and medium- to high-grade
79 metamorphic conditions. Rutile can readily crystallize from titanite, ilmenite and biotite during prograde metamorphism
80 (Luvizotto et al., 2009; Meinhold, 2010; Cave et al., 2015). The breakdown of rutile to titanite occurs in prograde and
81 retrograde environments, particularly in sub-greenschist to lower greenschist facies where titanite stability is favored (Cave et
82 al., 2015; Zack et al., 2004b). Experimentally, rutile is stable above around 1.2–1.4 GPa in metagranitoids and hydrated basalts
83 depending on compositional and chemical variability and in some cases can be stable down to 0.7 GPa (Xiong et al., 2005;
84 Angiboust and Harlov, 2017). In subduction zone settings, rutile is especially abundant in eclogites (Klemme et al., 2002).

85 The chemical composition of rutile preserves original petrogenetic information. Rutile concentrates high field
86 strength elements (Zr, Nb, Mo, Sn, Sb, Hf, Ta, W) through substitution with Ti that are commonly used as fingerprints of
87 subduction zone metamorphism and crustal evolution (Foley et al., 2000; Rudnick et al., 2000). Detrital rutile geochemistry
88 fingerprints the lithologies of sediment sources in several unique ways: rutile concentrates the vast majority of available Nb
89 whereas Cr is non-selective and is distributed across metamorphic minerals; therefore, the Cr and Nb concentrations in rutile
90 can discriminate between metamafic and metapelitic lithologies (Zack et al., 2004a, b; Triebold et al., 2011, 2012). Cr and Nb
91 concentrations are attributed to different protoliths: generally metapelitic rutile (i.e. mica schists, paragneisses, felsic
92 granulites) have less Cr than Nb contents, and metabasic rutile (i.e., mafic eclogites and granulites) have greater Cr than Nb
93 contents (Zack et al., 2004b). Additionally, the incorporation of Zr in rutile is largely temperature dependent (Zack et al.,

94 2004b; Watson et al., 2006; Tomkins et al., 2007; Ferry and Watson, 2007). Zirconium mobilizes during prograde metamorphic
95 fluid release; the incorporation of Zr into rutile is buffered by coexisting quartz and zircon (Zack et al., 2004b). Zr contents in
96 rutile correlate with peak metamorphic temperature and pressure conditions (Zack et al., 2004b; Watson et al., 2006; Tomkins
97 et al., 2007; Kohn, 2020). Therefore, the Zr elemental composition in rutile is a commonly used thermometer, empirically and
98 experimentally calibrated across a range of pressures and thermodynamic activity parameters (Zack et al., 2004b; Watson et
99 al., 2006; Tomkins et al., 2007; Kohn, 2020). Zircon, quartz and rutile must be in equilibrium to use the Zr-in-rutile
100 thermometer (e.g., Zack et al., 2004b), an assumption that likely holds in pelitic rocks (Pereira et al., 2021) but may not in
101 mafic lithologies, yet the assumption is hard to evaluate in a detrital context. Inclusions in rutile can be used to determine
102 whether rutile grew in equilibrium (Hart et al., 2016, 2018; see also Pereira and Storey, 2023 and references therein). In detrital
103 rutile, removed from the petrologic system in which they formed and thereby missing key thermobarometric mineral
104 associations, the Zr-in-rutile thermometer provides an estimate of the minimum peak metamorphic temperatures because the
105 exact activity of SiO₂ in the original system is unconstrained (Kooijman et al., 2012; Triebold et al., 2012; Pereira et al., 2021;
106 see also Meinhold et al., 2008; Rösel et al., 2019; Şengün et al., 2020; Zoleikhaei et al., 2021). For rutile of unknown source
107 lithology, the calculated temperature is affected by the chosen pressure estimate. Pereira and Storey (2023) demonstrate this
108 pressure dependence in detrital grains and recommend using the experimental and empirical calibration of Kohn (2020; their
109 eqn. 13) at an average pressure of 13 kbar with an uncertainty of 5 kbar:

$$110 \quad T \text{ (}^\circ\text{C)} = \frac{71360 + 0.378 \times P - 0.130 \times C}{130.66 - R \times \ln[C]} - 273.15$$

111 (1)

112 where P is the pressure in bars, C is the concentration of Zr in ppm and R is the gas constant, 8.3144 in J·mol⁻¹·K⁻¹.

113 Uranium is easily substituted for Ti⁴⁺ in rutile making rutile a suitable mineral for U-Pb analysis. Rutile U-Pb analyses
114 were first performed using thermal ionization mass spectrometry (TIMS) (Schärer et al., 1986; Mezger et al., 1989; Möller et
115 al., 2000; Schmitz and Bowring, 2003; Kylander-Clark et al., 2008) and have since been collected with SHRIMP (Clark et al.,
116 2000; Meinhold et al., 2010; Ewing et al., 2015), LA-MC-ICP-MS (Vry and Baker, 2006; Bracciali et al., 2013; Apen et al.,
117 2020), LA-Q-ICP-MS (Storey et al., 2007; Zack et al., 2011), and LA-SC-ICP-MS (Kooijman et al., 2010; Okay et al., 2011;
118 Smye and Stockli, 2014). As a high-temperature thermochronometer, U-Pb dates in rutile likely reflect mineral cooling through
119 the closure temperature for volume diffusion of Pb (Dodson, 1973), which is between 400–640°C in rutile. The temperature
120 sensitivity of this partial retention zone in rutile is dependent on diffusion kinetics, cooling rate, chemistry, and grain size
121 (Mezger et al., 1989; Cherniak, 2000). Rutile U-Pb dates may correspond to monotonic cooling from post-magmatic
122 temperatures or cooling from the most recent medium to high-temperature metamorphic event that exceeded the closure
123 temperature (Zack et al., 2004b; Zack and Kooijman, 2017). Slow cooling rates can produce rutile U-Pb dates significantly
124 younger than the timing of peak metamorphism (e.g., Möller et al., 2000; Flowers et al., 2005). Because rutile U-Pb dates
125 record thermal history information from conditions characteristic of the middle to lower crust (> 400 °C), U-Pb dates are ideal
126 for inferring the timing and rate of deep seated orogenic processes (Mezger et al., 1989; Möller et al., 2000; Flowers et al.,

2005; Kylander-Clark et al., 2008; Smye et al., 2018) and of craton formation, stabilization and cooling (Davis et al., 2003; Schmitz and Bowring, 2003; Blackburn et al., 2012). Furthermore, detrital rutile U-Pb geochronology is regularly used in sedimentary provenance analysis to reconstruct sedimentary basin evolution, paleoclimate and paleoenvironments, and orogen-scale deformation, exhumation, and sediment transport (Rösel et al., 2014, 2019; Mark et al., 2016; O’Sullivan et al., 2016; Pereira et al., 2020; Caracciolo et al., 2021; Clift et al., 2022).

2.2 Detrital Rutile U-Pb Challenge #1: Low Uranium Content

Detrital rutile U-Pb petrochronology presents unique analytical, data reduction, and interpretation challenges. Uranium concentration in rutile varies among metamorphic protoliths: for example, rutile from mafic eclogites tend to have, on average, 75% less U than those from metapelites (i.e., 5 ppm vs. 21 ppm; Meinhold, 2010). The low U concentrations— from old rutile or sourced from mafic lithologies (cf. Section 6.2)—can make rutile challenging to date. To optimize data collection, some detrital rutile methods first analyze trace elements then only collect U-Pb data on rutile above a given U concentration threshold (ca. > 4–5 ppm; e.g., Zack et al., 2004a, 2011; Okay et al., 2011; Rösel et al., 2019). There is not a systematic relationship between uranium concentration and common Pb concentration. However, screening low U rutile reduces the overall length of U-Pb analytical sessions and produces a higher proportion of concordant analyses (Zack et al., 2004a, 2011; Okay et al., 2011; Rösel et al., 2019). This protocol however introduces bias into the provenance results against metamafic rocks (cf. Section 6.2), and is generally discouraged (Bracciali et al., 2013; Bracciali, 2019). While this low-U screening is not necessarily common globally, it is a regional concern. There are 4 published detrital rutile U-Pb datasets from Türkiye; 2 of the 4 (Okay et al., 2011; Şengün et al., 2020) only analyze U-Pb on detrital rutile with uranium concentrations above ca. 4-5 ppm. The two studies that do not use a U-threshold filter but instead analyze all detrital rutile grains (Shaanan et al., 2020; this study) must discard data due to very low uranium signals (below limit of detection). This includes discarding rutile grains that have low incorporation of U during growth (independent of analytical instrumentation) and rutile grains that have poorly resolved U-Pb ratios due to low U CPS such as old rutile and mafic rutile (machine dependent). Omitting low U rutile may make sense in some settings; however, this analytical approach likely biases provenance results as the concentration of uranium in rutile systematically varies by metamorphic protoliths, with mafic eclogites having lower U contents than metapelites (e.g., Meinhold, 2010). This potential bias is important to investigate as metamafic units in suture zones, presumably with low U rutile, are expected to be a major contributor of detritus to many orogenic basins, including the northwestern Anatolian basins of this study.

2.3 Detrital Rutile U-Pb Challenge #2: Common Pb Incorporation

2.3.1 Common Pb Correction Overview

A second challenge with detrital rutile lies with data reduction and presentation. Because many detrital geochronologists are familiar with the zircon system, here we emphasize the differences in how U-Pb data should be treated

158 in common Pb bearing minerals versus zircon. The U-Pb system in rutile is different from that of zircon due to the incorporation
159 of common Pb, thereby requiring careful methodological choices on how to treat non-radiogenic Pb and U-Pb discordance.
160 The zircon U-Pb system is ‘simple’ in the sense that zircon incorporates negligible non-radiogenic initial Pb (i.e., common Pb)
161 during crystallization, and Pb diffuses only at extremely high temperatures and in zircon with radiation damage (e.g., Schoene,
162 2014 and references therein). Thus, the majority of detrital zircon U-Pb analyses tend to be close to concordia, which makes
163 data reduction and interpretation fairly straightforward, as even the $^{207}\text{Pb}/^{206}\text{Pb}$ dates of moderately discordant zircon are likely
164 to be meaningful. Unlike zircon where discordant data exceeding a specified threshold are often discarded, it is not surprising
165 that many rutile analyses may be discordant as rutile can incorporate a significant amount of common Pb. *In-situ* studies
166 mitigate this by: (1) regressing discordia lines through co-genetic analyses in Tera-Wasserburg space, where the lower intercept
167 of the discordia with the concordia defines the U-Pb age of Pb diffusion closure (e.g., Faure, 1986; Chew et al., 2011;
168 Vermeesch, 2020); or (2) applying a non-radiogenic Pb correction either by using an *ad hoc* Pb evolution model such as that
169 of Stacey and Kramers (1975) or by measuring the composition of non-radiogenic Pb in a co-existing phase (e.g. Zack et al.
170 2004b). However, by nature, co-genetic grains in detrital samples are unknown, and a model therefore has to be applied. Below
171 we review the common Pb correction calculations and discordance metrics for common Pb bearing detrital minerals.

172 2.3.2 ^{204}Pb Correction

173 The basis of all common Pb correction approaches— ^{204}Pb , ^{207}Pb and ^{208}Pb —is to use a Pb evolution model (e.g.,
174 Stacey and Kramers, 1975) to find the fraction of total ^{206}Pb that is common ^{206}Pb and, by corollary, find the radiogenic ^{206}Pb
175 fraction and then calculate the corrected date (Compston et al., 1984; Williams, 1997). We did not measure ^{204}Pb in this study
176 and refer readers to other publications for ^{204}Pb correction details (Williams, 1997; Andersen, 2002; Storey et al., 2006; Chew
177 et al., 2014). The ^{204}Pb correction method is valuable because it uses the non-radiogenic ^{204}Pb isotope and does not assume
178 concordance, yet accurate measurement of ^{204}Pb is needed (in contrast, see Andersen, 2002) which can be challenging as ^{204}Pb
179 is the least abundant Pb isotope. While accurate determination of the low-intensity ^{204}Pb peak is not a problem for TIMS or
180 MC-ICP-MS instruments (e.g., Simonetti et al., 2005; Gehrels et al., 2008), it can require prohibitively long dwell times in
181 single-collector instruments. Furthermore, the measurement of ^{204}Pb is complicated by the isobaric interference of ^{204}Hg
182 introduced in the gas supply. In some cases, the concentration of ^{204}Hg can be reduced with traps or filters and back stripped
183 by measuring ^{201}Hg or ^{202}Hg (e.g., Storey et al., 2006).

184 2.3.3 ^{208}Pb Correction

185 The ^{208}Pb correction method determines the common Pb component using the ^{232}Th - ^{208}Pb decay scheme and assumes
186 U-Th-Pb concordance, undisturbed Th/U, and no Pb loss. Because Pb loss is not considered, all corrected dates are (possibly)
187 minimum ages. The ^{208}Pb correction is ideal for low-Th phases (Zack et al., 2011) and is commonly used for rutile, although
188 not all rutile grains have low Th concentrations and Th contents are often not reported. The equations here are previously
189 described in Williams (1997), Chew et al. (2011), McLean et al. (2011) and as the total-Pb/U-Th scheme in Vermeesch (2020).

190 The proportion of $^{206}\text{Pb}_{\text{common}}$, f_{206} , is calculated as

$$191 \quad f_{206} = \frac{(^{208}\text{Pb}/^{206}\text{Pb}_{\text{measured}}) - (^{208}\text{Pb}^*/^{206}\text{Pb}^*)}{(^{208}\text{Pb}/^{206}\text{Pb}_{\text{common}}) - (^{208}\text{Pb}^*/^{206}\text{Pb}^*)}$$

192 (2)

193 where $^{208}\text{Pb}/^{206}\text{Pb}_{\text{measured}}$ is calculated directly from the raw data. The $^{208}\text{Pb}/^{206}\text{Pb}_{\text{common}}$ ratio is calculated from the two-stage
194 Pb evolution model of Stacey and Kramers (1975) for dates older than 3.7 Ga as

$$195 \quad \left(\frac{^{206}\text{Pb}}{^{204}\text{Pb}}\right)_{\text{common}} = 7.19 \cdot (e^{\lambda_{238} \cdot 4.57 \times 10^9} - e^{\lambda_{238} \cdot t_i}) + 9.307$$

196 (3)

197 and

$$198 \quad \left(\frac{^{208}\text{Pb}}{^{204}\text{Pb}}\right)_{\text{common}} = 33.21 \cdot (e^{\lambda_{232} \cdot 4.57 \times 10^9} - e^{\lambda_{232} \cdot t_i}) + 29.487$$

199 (4)

200 or for dates younger than 3.7 Ga as

$$202 \quad \left(\frac{^{206}\text{Pb}}{^{204}\text{Pb}}\right)_{\text{common}} = 9.74 \cdot (e^{\lambda_{238} \cdot 3.7 \times 10^9} - e^{\lambda_{238} \cdot t_i}) + 11.152$$

203 (5)

204 and

$$205 \quad \left(\frac{^{208}\text{Pb}}{^{204}\text{Pb}}\right)_{\text{common}} = 36.84 \cdot (e^{\lambda_{232} \cdot 3.7 \times 10^9} - e^{\lambda_{232} \cdot t_i}) + 31.23$$

206 (6)

207 where using t_i is the uncorrected date in years ($^{206}\text{Pb}/^{238}\text{U}$ date from the iolite data reduction), the ^{232}Th decay rate λ_{232} is
208 $4.9475 \times 10^{-11} \text{ yr}^{-1}$, and the ^{238}U decay rate λ_{238} is $1.55125 \times 10^{-10} \text{ yr}^{-1}$ (Faure, 1986). The expected radiogenic $^{208}\text{Pb}^*/^{206}\text{Pb}^*$ ratios
209 are calculated as

$$210 \quad \frac{^{208}\text{Pb}^*}{^{206}\text{Pb}^*} = \left(\frac{^{232}\text{Th}}{^{238}\text{U}}\right) \cdot \left(\frac{e^{\lambda_{232} t_i} - 1}{e^{\lambda_{238} t_i} - 1}\right)$$

211 (7)

212 Then, the radiogenic component, the $^{206}\text{Pb}^*/^{238}\text{U}$ ratio, can be calculated as

$$213 \quad ^{206}\text{Pb}^*/^{238}\text{U} = (1 - f_{206}) \cdot (^{206}\text{Pb}/^{238}\text{U}_{\text{measured}}).$$

214 (8)

215 Finally, the ^{208}Pb -corrected date ($^{206}\text{Pb}^*/^{238}\text{U}$ date) is calculated by solving the age equation with the $^{206}\text{Pb}^*/^{238}\text{U}$ ratio:

$$216 \quad t_{206} = \frac{1}{\lambda_{238}} \cdot \ln \left(\frac{^{206}\text{Pb}^*}{^{238}\text{U}} + 1 \right)$$

217 (9)

218 where t_{206} is the corrected date in years. The final corrected date is calculated iteratively, whereby each iteration replaces t_i
 219 with the previously calculated $^{206}\text{Pb}^*/^{238}\text{U}$ date. To test the sensitivity of the initial date estimate, we varied the initial date
 220 estimate, and therefore the initial common Pb composition, from 1 Ma to 1000 Ma and, by the fifth iteration, the resulting
 221 ^{208}Pb -corrected date differs by less than 0.05% for 98% of the unknowns. The final ^{208}Pb -corrected date presented here is from
 222 the two hundredth iteration. The uncertainty on the date is calculated as the equivalent of the percent (propagated) uncertainty
 223 of the uncorrected $^{206}\text{Pb}/^{238}\text{U}$ ratio (Odlum et al., 2019).

224 2.3.4 ^{207}Pb Correction

225 The ^{207}Pb correction method is based on a linear regression of $^{207}\text{Pb}/^{206}\text{Pb}$ and $^{238}\text{U}/^{206}\text{Pb}$ in Tera-Wasserburg space
 226 (Tera and Wasserburg, 1972) along a two-component mixing line between non-radiogenic and radiogenic Pb (Faure, 1986;
 227 Figure S7). This method is most powerful for co-genetic minerals because it does not require knowing $^{207}\text{Pb}/^{206}\text{Pb}_{\text{common}}$. Yet,
 228 because co-genetic analyses are inherently unknown in detrital samples, the routine used here calculates the common Pb
 229 component of each individual analysis using the Stacey and Kramers (1975) two-stage Pb evolution model and an initial age
 230 estimate. The ^{207}Pb correction method assumes U-Pb concordance and no Pb loss but, unlike the ^{208}Pb correction, does not
 231 assume an undisturbed U/Th ratio. Because Pb loss is not considered, all corrected dates are (possibly) minimum ages. The
 232 equations given here are modified for detrital samples with unknown co-genetic minerals, previously described in Faure
 233 (1986), Williams (1997), Chew et al. (2011), and the semitotal-Pb/U scheme of Ludwig (1998) and Vermeesch (2020).

234 The calculation is similar to the ^{208}Pb correction. First, the proportion of $^{206}\text{Pb}_{\text{common}}$ is calculated as

$$235 \quad f_{206} = \frac{(^{207}\text{Pb}/^{206}\text{Pb}_{\text{measured}}) - (^{207}\text{Pb}^*/^{206}\text{Pb}^*)}{(^{207}\text{Pb}/^{206}\text{Pb}_{\text{common}}) - (^{207}\text{Pb}^*/^{206}\text{Pb}^*)}$$

236 (10)

237 where $^{207}\text{Pb}/^{206}\text{Pb}_{\text{measured}}$ is taken directly from the raw data. The $^{207}\text{Pb}/^{206}\text{Pb}_{\text{common}}$ ratio is based on the two-stage Pb evolution
 238 model of Stacey and Kramers (1975), which is calculated as the ratio of Equation (3) and Equation (11) for dates older than
 239 3.7 Ga or as the ratio of Equation (5) to Equation (12) for dates younger than 3.7 Ga:

$$240 \quad \left(\frac{^{207}\text{Pb}}{^{204}\text{Pb}} \right)_{\text{common}} = \frac{7.19}{137.88} \cdot (e^{\lambda_{235} \cdot 4.57 \times 10^9} - e^{\lambda_{235} \cdot t_i}) + 10.294$$

241 (11)

242 or

$$\left(\frac{{}^{207}\text{Pb}}{{}^{204}\text{Pb}}\right)_{\text{common}} = \frac{9.74}{137.88} \cdot (e^{\lambda_{235} \cdot 3.7 \times 10^9} - e^{\lambda_{235} \cdot t_i}) + 12.998$$

(12)

where t_i is the initial date estimate in years and the ${}^{235}\text{U}$ decay rate λ_{235} is $9.8485 \times 10^{-10} \text{ yr}^{-1}$ (Faure, 1986). Here, for t_i we use the ${}^{206}\text{Pb}/{}^{238}\text{U}$ date from the iolite data reduction. However, Chew et al. (2011) demonstrated that the choice of initial date results in a $< 0.05\%$ difference in the final ${}^{207}\text{Pb}$ -corrected date after 5 iterations. The expected radiogenic ${}^{207}\text{Pb}/{}^{206}\text{Pb}^*$ ratio is calculated as

$$\frac{{}^{207}\text{Pb}^*}{{}^{206}\text{Pb}^*} = \left(\frac{{}^{235}\text{U}}{{}^{238}\text{U}}\right) \cdot \left(\frac{e^{\lambda_{235} t_i} - 1}{e^{\lambda_{238} t_i} - 1}\right)$$

(13)

where ${}^{235}\text{U}/{}^{238}\text{U}$ is 137.88 (Steiger and Jäger, 1977). Finally, the radiogenic component, the ${}^{206}\text{Pb}^*/{}^{238}\text{U}$ ratio, can be calculated using Equation (8) and then used to solve the age equation (Equation (9)). As with the ${}^{208}\text{Pb}$ correction, to iteratively calculate the date, each iteration replaces t_i with the previously calculated ${}^{206}\text{Pb}^*/{}^{238}\text{U}$ date. The ${}^{207}\text{Pb}$ -corrected date presented here is from the two hundredth iteration. The uncertainty on the date is calculated as the equivalent of the percent (propagated) uncertainty of the uncorrected ${}^{206}\text{Pb}/{}^{238}\text{U}$ ratio (Odlum et al., 2019). For example, if the initial ${}^{206}\text{Pb}/{}^{238}\text{U}$ ratio has 2% uncertainty at 2 sigma and the corrected date is 200 Ma, then the corrected date uncertainty is $\pm 4 \text{ Ma}$ (2s).

2.3.5 Discordance

Although there are various ways to calculate the discordance of U-Pb analyses, which are reviewed elsewhere (e.g., Vermeesch, 2021), it remains unclear which metric is best for common Pb bearing minerals and if a discordance threshold should be applied. One family of discordance metrics relies on the difference between the ${}^{206}\text{Pb}/{}^{238}\text{U}$ date and ${}^{207}\text{Pb}/{}^{206}\text{Pb}$ date (e.g., Gehrels, 2011). Because ${}^{207}\text{Pb}$ and ${}^{208}\text{Pb}$ corrections force concordance, these metrics are not applicable to common Pb bearing minerals. One metric potentially relevant to common Pb-bearing minerals is the Stacey-Kramers distance (after Vermeesch, 2021; see Text S3 for further discussion). The Stacey-Kramers distance is calculated by first using the U-Pb analysis and ${}^{207}\text{Pb}/{}^{206}\text{Pb}_{\text{common}}$ composition (calculated during common Pb correction) to find the discordia in Tera-Wasserburg space, then discordance is calculated as the distance between the measured ${}^{238}\text{U}/{}^{206}\text{Pb}$ and ${}^{207}\text{Pb}/{}^{206}\text{Pb}$ coordinates and the concordia intersection (δ_2) along the total discordia line distance ($\delta_1 + \delta_2$) (Figure S7; Vermeesch, 2021):

$$\text{Concordance} = \delta_1 / (\delta_1 + \delta_2)$$

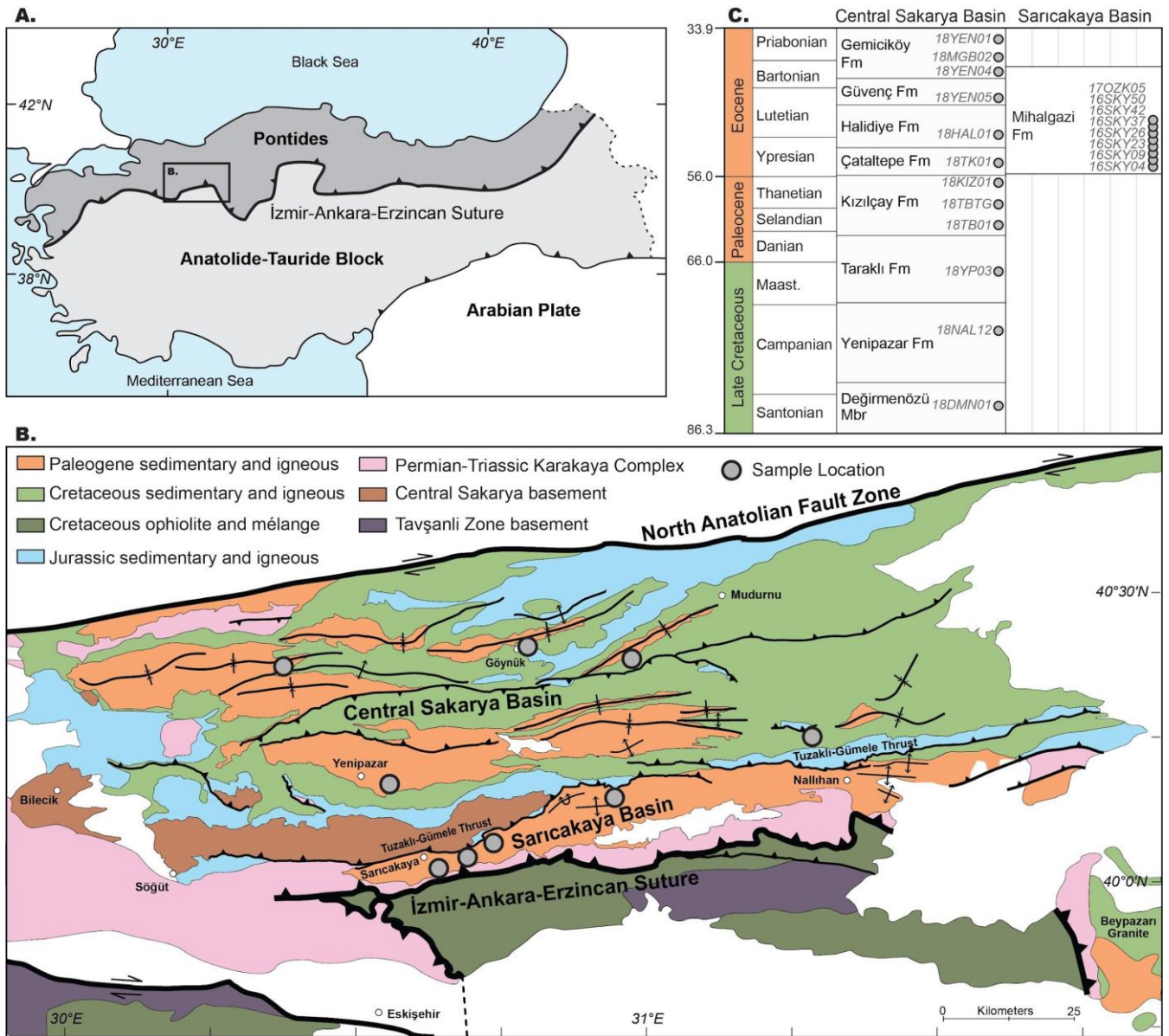
(14)

If a discordance threshold is applied, the Stacey-Kramers distance approach includes more young dates than old dates ($> 1000 \text{ Ma}$) due to the change in concordia slope around 1000 Ma (Figure S7; Vermeesch, 2021). The application of a discordance threshold has been underexplored in detrital rutile, with most studies applying no discordance filter, perhaps due to the lack of consensus on how to define discordance in common Pb bearing minerals. Rather, a group of studies proposes to filter analyses

273 based on the percent uncertainty of the corrected date (Mark et al., 2016; Govin et al., 2018; Chew et al., 2020; Caracciolo et
274 al., 2021). It is noted that there is little guidance on how uncertainties are calculated and propagated during Pb correction,
275 which ought to be investigated in future work; meanwhile, the filters should be applied with care. We explore these thresholds
276 with our new dataset.

277 **3. Geologic Context**

278 Anatolia is composed of a series of subduction complexes, island arcs, and continental terranes that accreted and
279 collided from the Late Paleozoic through Cenozoic during the progressive opening and closing of Paleotethys and Neotethys
280 seaways (Şengör and Yilmaz, 1981). Today, northwestern Anatolia comprises, from structurally highest (north) to lowest
281 (south), the continental Pontides, including the Cretaceous–Eocene forearc-to-foreland Central Sakarya and Sarıcakaya Basins,
282 the Permian–Triassic Karakaya Complex, the İzmir-Ankara-Erzincan suture zone and associated Neotethys ophiolites and
283 mélange, and the lower plate Anatolide-Tauride continental terranes (Figure 1). The Pontides basement contains Paleozoic
284 paragneiss, schist, and amphibolite rocks intruded by Carboniferous granitoids emplaced during the Variscan orogeny
285 (Göncüoğlu et al., 2000; Ustaömer et al., 2012). The nature of the Karakaya Complex is debated but is generally considered a
286 subduction-accretion complex associated with the Late Paleozoic–Early Mesozoic closure of the Paleotethys along the
287 southern margin of Eurasia (Pickett and Robertson, 1996; Okay and Göncüoğlu, 2004; Federici et al., 2010; Ustaömer et al.,
288 2016). The Karakaya Complex contains metamafic and metasedimentary rocks interpreted as seamounts of intra-oceanic
289 basaltic composition and forearc basin and trench deposits (Pickett and Robertson, 1996) that were subsequently
290 metamorphosed to blueschist and epidote-amphibolite with minor eclogite facies with estimated temperatures of $340\text{--}550 \pm$
291 $50 \text{ }^\circ\text{C}$ (Okay et al., 2002; Federici et al., 2010) with phengite, glaucophane, and barroisite Ar-Ar cooling dates around 200–
292 215 Ma (Okay et al., 2002). The youngest Karakaya Complex units are unmetamorphosed or metamorphosed to zeolite to
293 lower greenschist facies ($120\text{--}376 \text{ }^\circ\text{C}$) (Federici et al., 2010) and are unconformably overlain by Jurassic platform carbonates.
294 The Cretaceous to present closure of the Neotethys and associated suturing is recorded in the Central Sakarya and Sarıcakaya
295 Basins located north of the suture zone. Stratigraphic and paleocurrent (Ocakoglu et al., 2018), provenance (Mueller et al.,
296 2022; Campbell et al., 2023), and mudstone geochemistry records (Açıklalın et al., 2016) show the input of suture zone derived
297 material into the Central Sakarya Basin from the Late Cretaceous through Eocene, interpreted as progressive suture zone uplift
298 and exhumation during continental collision (Ocakoglu et al., 2018; Okay et al., 2020; Mueller et al., 2022; Campbell et al.,
299 2023). Cretaceous subduction-related arc volcanism and Paleogene syn-collisional volcanic centers are located within and to
300 the north of the basins (Kasapoğlu et al., 2016; Ersoy et al., 2017, 2023; Keskin and Tüysüz, 2018). By Eocene times, continued
301 collision increased plate coupling which manifested as increased contractional deformation that activated the basement-
302 involved Tuzaklı-Gümele Thrust (also termed the Söğüt Thrust or Nallıhan Thrust) and partitioned the southern Central
303 Sakarya Basin into the Sarıcakaya Basin (Mueller et al., 2022). The Eocene Sarıcakaya Basin received sediment from the
304 suture zone and Karakaya Complex to the south and basement-involved thrust sheets to the north (Mueller et al., 2019).



305

306 Figure 1: (A) Simplified terrane map of Anatolia and (B) geologic map of the Central Sakarya Basin and Sarıcakaya Basin
 307 region (after Aksay et al., 2002). (C) Simplified stratigraphic correlation chart and schematic sample distribution. Stratigraphy
 308 after Ocakoğlu et al. (2018).

309 4 Methods

310 4.1 Sample Information

311 Sedimentary rock samples were collected from Upper Cretaceous to Eocene siliciclastic sections in the Central
312 Sakarya Basin and Sarıcakaya Basin in western Anatolia (Figure 1; Table S1). Detrital zircon U-Pb ages and Hf isotopes from
313 these samples are already published (cf. Section 8; Mueller et al., 2019, 2022; Campbell et al., 2023); a set of 20 samples were
314 chosen for detrital rutile U-Pb and trace element analyses. Heavy minerals were extracted using standard heavy mineral
315 techniques, including crushing, water table, heavy liquid, and magnetic separation (see supporting information). Rutile grains
316 were handpicked from the ≥ 0.3 amp. magnetic fraction using a Leica M205C binocular microscope. Three samples—
317 16SKY26, 16SKY42 and 17OZK05—yielded hundreds of rutile grains and we handpicked 260–320 rutile grains from each
318 sample, whereas all grains were picked from samples with smaller yield. The low yield of rutile grains partially contributes to
319 the low-*n* date distributions of the individual samples. Rutile grains were mounted in epoxy and polished to expose the internal
320 structure. Rutile mounts were carbon coated and imaged with a TFS Apreo-S with Lovac SEM with an energy-dispersive
321 detector (EDS) to distinguish TiO₂ grains from other heavy minerals (Figure S1).

322 4.2 U-Pb Analytical Protocol

323 Detrital rutile U-Pb geochronology was conducted at the Isotope Geochemistry Lab at the University of Kansas (KU-
324 IGL) using a Thermo Element2 magnetic sector field ICP-MS coupled to a Photon Machines AnalyteG2 excimer laser ablation
325 system. The protocol was modified from Rösel et al. (2019) to optimize for low U contents (Text S1; Table S2). The ICP-MS
326 was manually tuned using NIST SRM 612 reference material glass to optimize for high sensitivity and low oxide production.
327 Grains were ablated for 25 seconds with a laser beam diameter of 50 μm , laser fluence of 3.0 J/cm², and 10 Hz repetition rate.
328 The U-Pb data were collected in 4 analytical sessions. The analytical protocol was modified from session to session to optimize
329 for the analysis of low U and Pb unknowns and high U and Pb reference materials. In the first two analytical sessions, 21RtF
330 and 21RtG, Pb and Th isotopes were measured with the secondary electron multiplier operating in counting detection mode,
331 whereas Pb and Th isotopes were measured with the secondary electron multiplier in both counting and analog modes ('both
332 mode') for the final two sessions, 21RtA and 21RtB. Primary and secondary reference materials were the R10 (1091.6 \pm 3.5
333 Ma by TIMS, 2s abs.; Luvizotto et al., 2009), Wodgina (2845.8 \pm 7.8 Ma by TIMS; Ewing, 2011), 9826J (381.9 \pm 1.1 Ma by
334 TIMS; Kylander-Clark, 2008), LJ04-08 (498 \pm 3 Ma by LA-ICP-MS; Apen et al., 2020), and Kragerø (1085.7 \pm 7.9 Ma by
335 TIMS; Kellett et al., 2018). For U-Pb analyses, the analysis of 5-8 unknowns was followed by 2 standards, the primary standard
336 R10 and one of the secondary standards. The data were reduced in iolite 4 (Paton et al., 2011), calibrated against R10
337 uncorrected for initial Pb, and using the weighted linear fit drift correction which reproduced secondary standard ages and
338 brought their MSWDs closest to 1. The concordia ages are satisfactory for all reference materials, except for the Wodgina and
339 Kragerø, which did not perform well during the first two analytical sessions—likely due to ²⁰⁶Pb counts per second exceeding
340 the limit of linear behavior in counting detection mode—and are discarded from those analytical sessions. Standard

341 reproducibility is discussed further in the supplemental text included in the data repository; U-Pb data are provided in the data
342 repository (Mueller et al., 2023).

343 **4.3 Trace Element Geochemistry Analytical Protocol**

344 Detrital rutile trace element geochemistry (^{49}Ti , ^{51}V , ^{53}Cr , ^{66}Zn , ^{69}Ga , ^{90}Zr , ^{93}Nb , ^{95}Mo , ^{118}Sn , ^{121}Sb , ^{177}Hf , ^{181}Ta , ^{182}W)
345 was conducted at the KU-IGL using the same instrumentation and parameters, except with a 25 or 35 μm spot size. Reference
346 materials included USGS GSD-1G and USGS GSC-1G glasses (Jochum et al., 2011) and R10 rutile (Luvizotto et al., 2009).
347 For trace element analysis, the analysis of 5–10 unknowns was followed by analysis of 2 standards, the primary standard GSD-
348 1G and one of the secondary standards. Trace element concentrations were calculated using the Trace Element routine in iolite
349 4 with ^{49}Ti as an internal standard; for rutile unknowns, TiO_2 was set to be 100 mass-% (e.g., Plavsa et al., 2018; Rösel et al.,
350 2019). Standard reproducibility is discussed in the supporting information in the data repository (Text S2). In short, for the
351 secondary standard GSC-1G, all elements are within 10% of the published values except for Sn and Ga, and for the secondary
352 standard R10, all results are within the range of reported values. Following U-Pb and trace element analysis, mounts were
353 imaged in an SEM at University of Nevada Reno (Figure 2). Most grains have both U-Pb and trace element results, but some
354 grains have only U-Pb results due to the grains being too small for a second ablation spot or only trace element results due to
355 discarded U-Pb data. Detrital rutile trace element data are given in the data repository (Mueller et al., 2023).

356 **4.4 Additional Data Workflows**

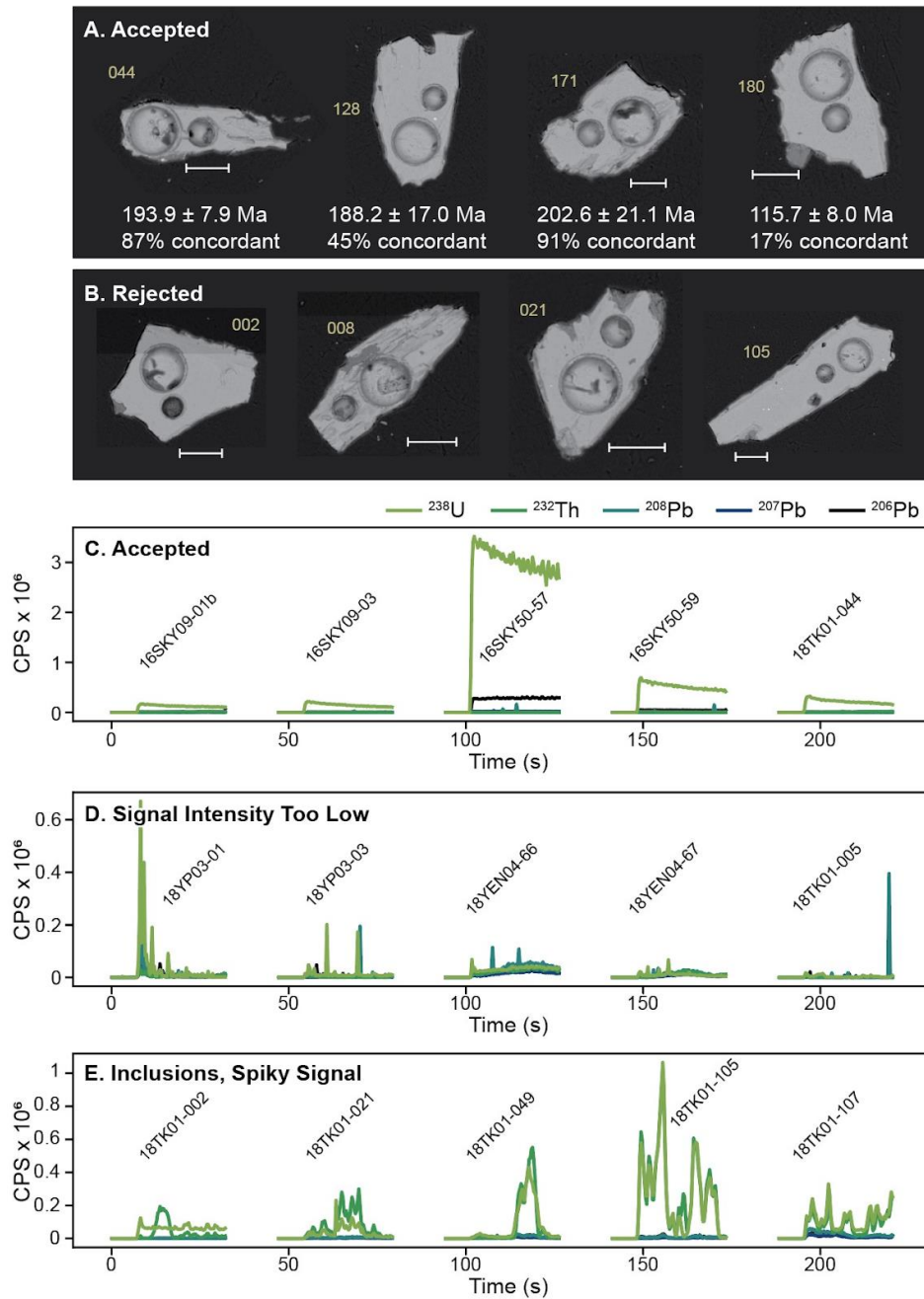
357 Additional data reduction and data calculations steps were performed. Provided as a complement to this manuscript
358 are open access Jupyter Notebooks that contain the Python and R code used to perform these additional calculations and to
359 generate figures, which are briefly described here (Mueller, 2024). (1) The ^{208}Pb and ^{207}Pb corrections were performed in the
360 Detrital-Common-Pb-Corrections notebook using the equations detailed in Section 2 above. The notebook allows for either a
361 manually set number of iterations or to iterate until all analyses are below a given threshold—the percent difference in corrected
362 date between the current and previous iteration. Presented here are the results from the 200th iteration. (2) The UPb-Plotter
363 notebook visualizes uncorrected U-Pb results in Tera-Wasserburg space, compares metrics for excluding analyses based on
364 uncertainty filters (Section 5.3), and calculates discordance using the Stacey-Kramers and Aitchison distances (Section 2; Text
365 S3; Figures S7-S8). (3) The Rutile-Trace-Elements notebook includes the calculations and resulting figures for exploring TiO_2
366 polymorphs, mafic and pelitic protoliths, Zr-in-rutile thermometry, and low U contents. Discrimination diagrams using V, Cr,
367 Zr, Fe, and Nb distinguish rutile from other TiO_2 polymorphs (Triebold et al., 2011), and all analyzed grains plot within the
368 rutile field (Figure S2). Rutile grains are classified as mafic or pelitic based on the Cr-Nb discrimination fields of Triebold et
369 al. (2012), and Zr-in-rutile temperatures are calculated with the Kohn (2020) formulation (Equation (1)) at 13 kbar. (4) The
370 Detrital-PCA-R notebook performs principal component analysis on trace element data using the `pcaCoDa` function in the
371 `robCompositions` library, which is designed to handle compositional data (Templ et al., 2011). (5) Additionally, the UPb-
372 Timeseries notebook is provided for visualizing U-Pb timeseries data.

373 5 U-Pb Geochronology Results

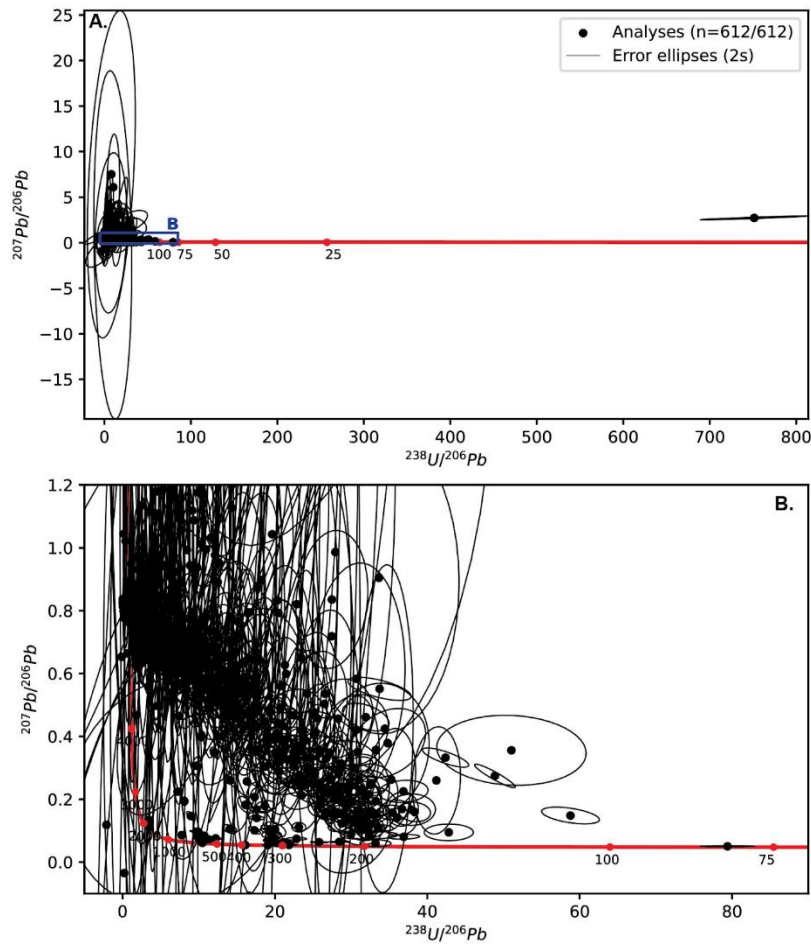
374 5.1 U-Pb Data Quality

375 A total of 1,278 detrital rutile grains were analyzed for U-Pb geochronology. A significant number of analyses were
376 rejected and excluded, as discussed below. We aim to be transparent in data reporting—including the number of grains
377 analyzed and the criteria for rejection—in order to give precedence for this practice, which is missing in the literature, and to
378 explore the current limitations of large-*n* detrital rutile studies. Even with the optimized LA-ICP-MS protocol, a significant
379 number of analyses did not meet quality control goals: 665 of 1,277 (54%) analyses were rejected due to anomalous (spiky)
380 patterns in raw signal intensity, or low U or low Pb signal intensity. Figure 2 depicts representative examples of signal intensity
381 in accepted and rejected analyses. Inclusions and anomalous patterns were easily spotted through monitoring ^{206}Pb , ^{207}Pb , ^{238}U ,
382 ^{232}Th , $^{206}\text{Pb}/^{238}\text{U}$ and $^{207}\text{Pb}/^{206}\text{Pb}$ channels. In some instances, the signal of an inclusion or anomalous (spiky) pattern was short
383 enough that the integration window could be shortened to exclude it. In other cases, the non-inclusion signal could not be
384 isolated and the entire analysis was discarded. Potential causes for the abnormal signal patterns and high Pb uncertainty include
385 (1) elemental heterogeneity from ablating into small inclusions and/or lamellae; (2) inhomogeneities due to micro-cracks with
386 different element/isotope composition; (3) heterogeneous amount of common lead incorporation during rutile growth; (4)
387 textural and/or elemental heterogeneities due to multiple rutile growth events. Although, scenarios 3 and 4 are unlikely for Pb
388 because it diffuses and should not cause spikes.

389 The SEM images do not give a clear picture of how to better select grains that will produce acceptable signal intensity
390 and U-Pb concordance. Figure 2 shows SEM images of representative rutile grains after laser ablation. All grains appeared
391 inclusion-free before ablation, yet some analyses clearly ablated into inclusions (Figure 2b,e). The large laser spot size of 50
392 μm gives a higher signal, which is better for grains with potentially low U or low Pb concentrations, but the potential trade-off
393 is increasing the likelihood of hitting inclusions. Grains with obvious inclusion lamellae generally yielded poor data quality.



394 *Figure 2: SEM BSE images and U-Pb signal intensities of representative rutile grains. (A) Rutile grains with acceptable U-*
 395 *Pb analyses across a range of concordance. U-Pb date and concordance are from the ^{207}Pb correction method and Stacey-*
 396 *Kramers metric, respectively. Ablation pits are from U-Pb analysis (larger) and trace element analysis (smaller). The scale*
 397 *bar is 50 μm . All grains are from sample 18TK01; the grain number is in yellow. (B) Images of rutile grains with U-Pb analyses*
 398 *rejected because of inclusions (18TK01-002) or spiky signal (18TK01-008, -021, -105). (C-E) Representative U-Pb raw signal*
 399 *intensity patterns of accepted analyses (C) and rejected analyses from too low signal intensity (D) or inclusions and/or spiky*
 400 *signal (E).*



401

402 *Figure 3. Uncorrected detrital rutile U-Pb results displayed in Tera-Wasserburg space. Uncertainty ellipses are 2s*
 403 *propagated. The area displayed in (B) is highlighted by the blue box in (A).*

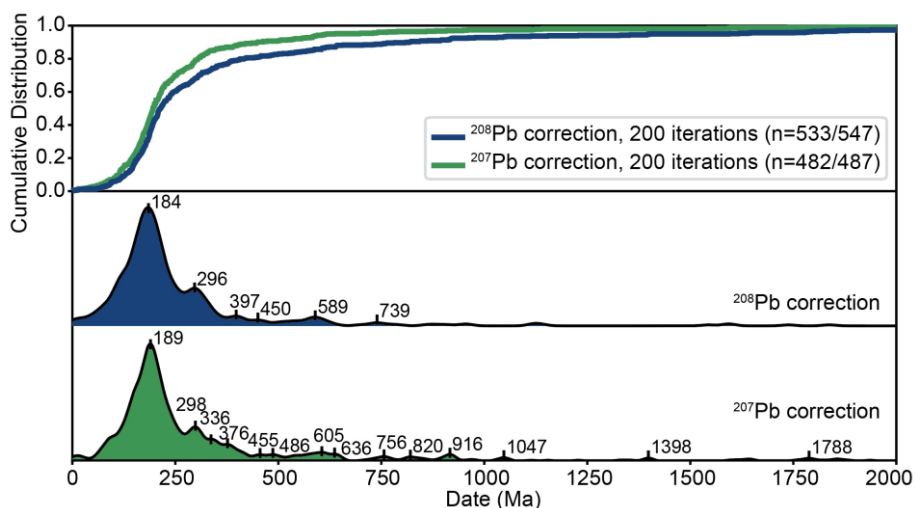
404 5.2 U-Pb Geochronology and Common Pb Correction Results

405 The uncorrected U-Pb results are displayed in Figure 3. We note that all concordia diagram figures display the
 406 uncorrected U-Pb data; common Pb corrections force concordance and the corrected data are displayed as date distributions.
 407 A number of analyses plot close to the concordia curve and many plot along the discordia trend toward common Pb values.
 408 Both ^{208}Pb - and ^{207}Pb -corrections were performed on the uncorrected U-Pb analyses. After 200 iterations, the ^{208}Pb - and ^{207}Pb -
 409 corrections resulted in 547 and 487 corrected dates between 0 Ma and 4500 Ma, respectively. These numbers differ because
 410 no corrected date is calculated when the proportion of $^{206}\text{Pb}_{\text{common}}$ is greater than 1, and because the common Pb corrections
 411 can yield dates younger than 0 Ma or significantly older than 4500 Ma depending on the calculated proportion of $^{206}\text{Pb}_{\text{common}}$
 412 (f_{206}). The Pb corrected U-Pb data are shown in Figure 4 as kernel density estimates (KDEs) and cumulative distributions. The

413 date distributions of individual samples are given in Figure S9, but due to small sample sizes, interpretations are based on the
414 cumulative dataset.

415 The two different Pb corrections produce similar date distributions (Figure 4). For both distributions, the main date
416 peak is at ca. 185 Ma with a minor peak around 297 Ma. The ^{207}Pb and ^{208}Pb distributions vary in the presence and amplitude
417 of minor Paleozoic and older populations. The ^{208}Pb correction results include more Devonian and older grains ($n=131/547$,
418 24%) than the ^{207}Pb correction ($n=68/487$, 14%).

419



420

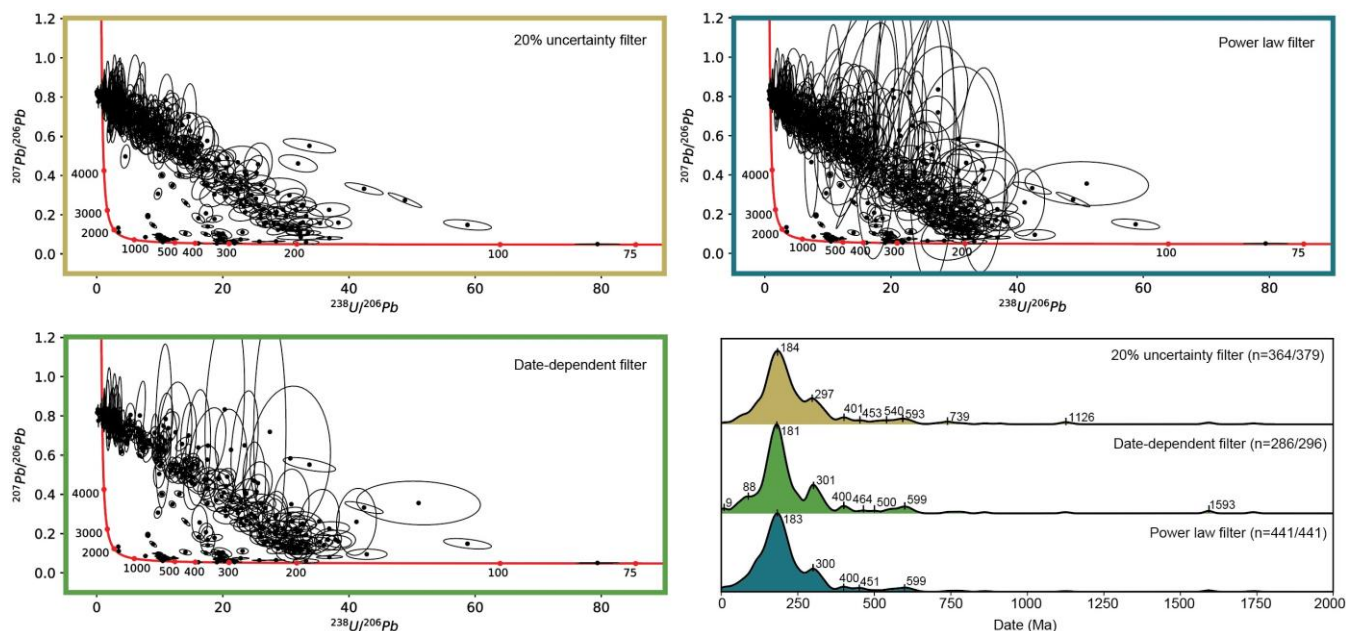
421 *Figure 4. The ^{208}Pb and ^{207}Pb corrected date distributions from 0 to 2000 Ma displayed as normalized kernel density estimates
422 and cumulative distributions, visualized with detritalPy (Sharman et al., 2018). No discordance or uncertainty filter is applied.*

423 5.3 Uncertainty and Discordance Thresholds

424 Detrital U-Pb data can further be filtered by U-Pb ratio uncertainty, date uncertainty, or discordance thresholds.
425 Because the uncertainty on the corrected date is calculated from the uncertainty on the measured $^{206}\text{Pb}/^{238}\text{U}$ ratio (cf. Section
426 2), these metrics are similar. Figure 5 displays the results of three uncertainty threshold filters: (1) 20% uncertainty on
427 $^{238}\text{U}/^{206}\text{Pb}$ and $^{207}\text{Pb}/^{206}\text{Pb}$ ratios (modified from Lippert, 2014), (2) a date-dependent filter that excludes analyses with > 10%
428 date uncertainty for corrected dates > 100 Ma, > 20% uncertainty for dates 10–100 Ma, or > 25% uncertainty for dates < 10
429 Ma (after Govin et al., 2018), and (3) a power law threshold that excludes analyses if the percent uncertainty on the ^{207}Pb
430 corrected date exceeds the function: $(t \wedge -0.65) * 8$ (after Chew et al., 2020). The results of these filters are displayed as
431 uncorrected U-Pb data in Tera-Wasserburg space and ^{207}Pb corrected date distributions (Figure 5). From the total ^{207}Pb
432 corrected analyses ($n=487$), the above thresholds exclude an additional 108 (22%), 191 (39%), and 46 (9%) analyses,
433 respectively. The power law function excludes the fewest number of analyses.

434 The three filters have similar ^{207}Pb corrected date distributions (Figure 5). The main age modes identified in all three
435 filters are 183 Ma, 300 Ma and 400 Ma. Minor Devonian and older date modes are present. Only the date-dependent filter
436 identifies the 89 Ma date mode and it includes a 9 Ma mode that is significantly younger than the youngest sampled strata

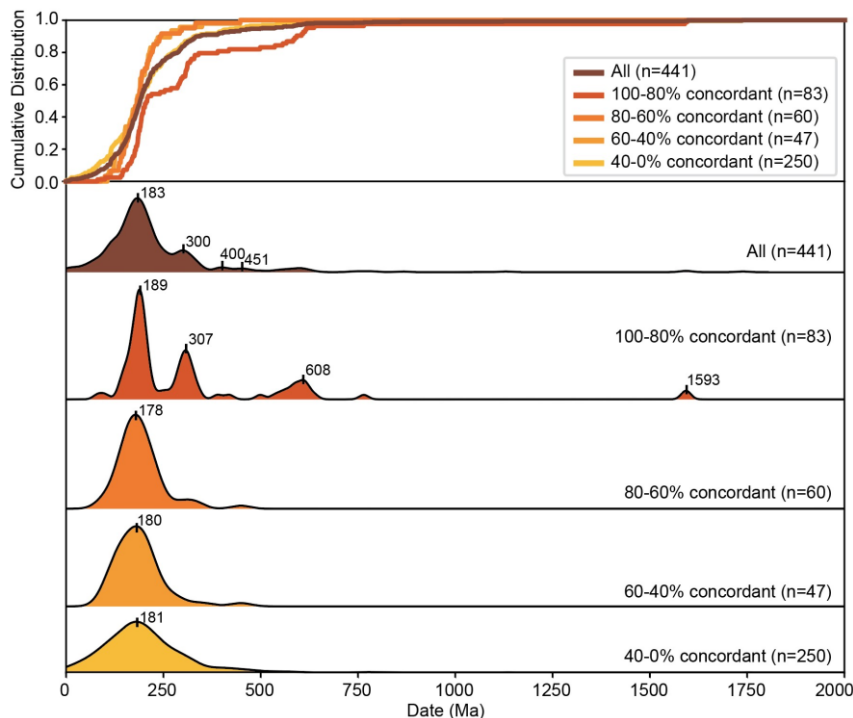
437 (Bartonian–Priabonian). The U-Pb ratio uncertainty and power law filters have nearly identical date peaks with the power law
 438 filter including more grains, especially in the ~183 Ma mode.
 439



440
 441 *Figure 5. Comparison of U-Pb data filters based on U-Pb ratio and date uncertainties, displayed in Tera-Wasserburg space*
 442 *(uncorrected) and normalized kernel density estimates (²⁰⁷Pb-corrected). The U-Pb ratio uncertainty filter (yellow) excludes*
 443 *all analyses with ²³⁸U/²⁰⁶Pb and ²⁰⁷Pb/²⁰⁶Pb ratio uncertainties above 20% (modified from Lippert, 2014). The date -dependent*
 444 *filter (green) excludes analyses based on the ²⁰⁷Pb-corrected date and uncertainty (see text; after Govin et al., 2018); after*
 445 *Govin et al., 2018). The power law filter (blue) excludes analyses if the percent uncertainty on the ²⁰⁷Pb corrected date exceeds*
 446 *the given power law function (see text; after Chew et al., 2020).*

447
 448 The Stacey-Kramers distance is used to quantify discordance in common Pb bearing minerals (Text S3; Figure S7).
 449 The results are shown in Figure S8 in Tera-Wasserburg space with uncorrected U-Pb analyses colored by distance
 450 (concordance). In the Stacey-Kramers distance formulation, analyses closest to the common Pb composition are considered
 451 most discordant (Figures S7 and S8). The Stacey-Kramers distance appears to reflect U-Pb systematics in common Pb bearing
 452 minerals and is a representative metric of discordance. Figure 6 displays the ²⁰⁷Pb-corrected date distributions filtered using
 453 the power law threshold and subdivided into bins based on their Stacey-Kramers concordance values. The 100-80%
 454 concordance group has the most discrete date modes at 189 Ma, 307 Ma, 608 Ma, and 1593 Ma. The 80-60%, 60-40% and 40-
 455 0% bins have unimodal age distributions that are asymmetric toward older dates, and have a dominant age mode around 180
 456 Ma. The cumulative distributions reveal that the distribution of all grains together has a similar distribution to that of the 40-
 457 0% group (Figure 6 top). Comparison of the distribution of all grains together to the 100-80% concordance group reveals that,
 458 if a 20% discordance filter were applied similar to detrital zircon U-Pb workflows, the same general date modes would be

459 identified. However, the addition of lower concordance grains (i.e., 80-0% concordance groups) broadens the Jurassic peak
 460 and shifts it slightly younger from 189 Ma to ~180 Ma, decreases the amplitude of the Carboniferous and Proterozoic peaks,
 461 and increases the amplitude of the ~400-450 Ma peaks.
 462

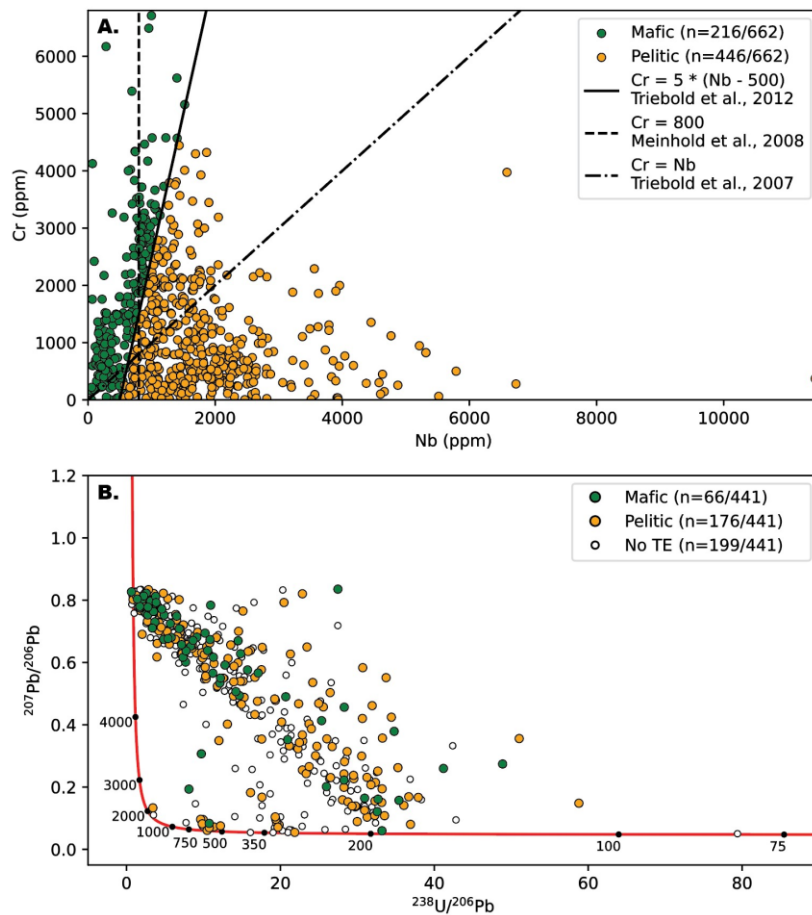


463 *Figure 6. Relative kernel density estimates (KDEs; bottom panels) and cumulative distributions (top) of ²⁰⁷Pb-corrected, power*
 464 *law uncertainty filtered dates categorized by discordance from Stacey-Kramers distance values.*
 465

466 6 Trace Element Geochemistry Results

467 6.1 Metamorphic Protolith

468 The Cr and Nb concentrations discriminate between metapelitic and metamafic source rocks (Zack et al., 2004a;
 469 Triebold et al., 2011, 2012). Even though there are multiple proposed discrimination lines between metamafic and metapelitic
 470 source lithologies (e.g., Meinhold et al., 2008; Triebold et al., 2012), the detrital rutile in this dataset plot in both the metamafic
 471 (33%) and metapelitic (67%) fields (Figure 7a). There is no clustering of protolith by U-Pb date, with prominent date modes
 472 containing both metamafic and metapelitic grains (Figure 7b). While some metamafic grains plot close to concordia (more
 473 concordant), many plot close to the common Pb composition concordia intercept (more discordant).



474

475 *Figure 7. (A) Protolith discrimination diagram. Grains are classified as (meta)mafic and (meta)pelitic based on the Triebold*
 476 *et al. (2012) line, with the Triebold et al. (2007) and Meinhold et al. (2008) lines also shown. (B) Concordia diagram of*
 477 *uncorrected U-Pb circles colored by protolith classification. The power law filter is applied. Open circles represent grains*
 478 *with U-Pb data but no trace element data (TE). Sample size differs between plots because not all grains have both U-Pb and*
 479 *trace element data.*

480 **6.2 Zr-in-Rutile Temperature and Uranium Concentration**

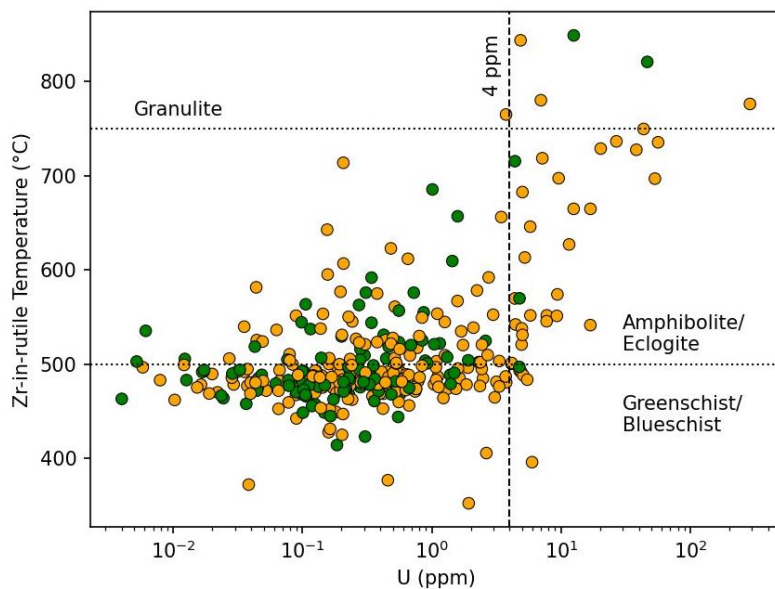
481 The Zr-in-rutile temperatures were calculated using the Kohn (2020) calibration (Equation (1)) at 13 kbar with an
 482 uncertainty of 5 kbar; results are included in the data repository. The Zr concentrations range from 2 to 1934 ppm, yielding
 483 source rock minimum peak temperatures from 336 ± 15 °C to 849 ± 28 °C. The Zr-in-rutile temperature results are displayed
 484 alongside U concentration and colored by protolith (Figure 8). There is not a correlation between Zr-in-rutile temperature and
 485 protolith. The majority of grains have moderate temperatures corresponding to greenschist to blueschist facies conditions: 68%
 486 (n=147/216) of mafic and 67% (n=301/446) of pelitic grains are below 500 °C. There are fairly consistent Zr-in-rutile
 487 temperatures within the dominant date modes—90 Ma, 185 Ma, 300 Ma, 500–650 Ma (Figure 9). The highest temperatures,
 488 reaching granulite facies conditions, are found in the 90 Ma date mode. The 500–650 Ma and 300 Ma rutile grains similarly

489 preserve high temperatures, up to 700–820 °C, whereas the majority of 185 Ma grains have temperatures in greenschist to
490 blueschist facies around 450–550 °C.

491 The uranium concentrations range from 0.002 to 113 ppm. These low values are above the detection limit. The
492 primary standard, R10, has a U concentration of 44 ppm (Luvizotto et al., 2009) and, in our measurements, on average, 2.1
493 million CPS ^{238}U (i.e., ~50,000 counts/ppm). The ^{238}U baseline was about 5 CPS, therefore, the instrument set-up has a
494 detection limit of about 0.0003 ppm ^{238}U (calculated from 3x background). All analyses are above the detection limit, with
495 91% (n=555/612) of analyses at least an order of magnitude above this limit.

496 The comparison of Zr-in-rutile temperatures with U concentration reveals that the majority of low U rutile (< 4 ppm)
497 are within greenschist to blueschist facies conditions (68%, n=205/303 below 500 °C; Figure 8). Additionally, mafic classified
498 grains are dominantly low U (95%, n=106/112 below 4 ppm). The majority of rutile with U contents above 4 ppm are classified
499 as pelitic (85%, n=34/40) and generally have higher Zr contents.

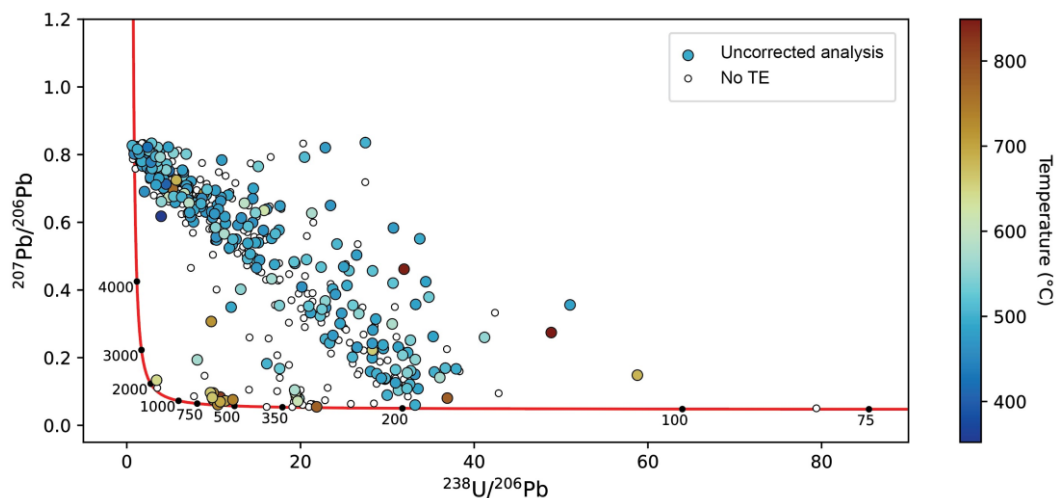
500



501

502 *Figure 8. Zr-in-rutile temperature versus U concentration. Mafic and pelitic discrimination is from Cr and Nb concentrations*
503 *(Figure 7) mafic protoliths shown in green, pelitic in orange. The 4 ppm U line demarcates grains included/excluded by a U*
504 *filter. Zr-in-rutile temperatures follow the Kohn (2020) calibration. Note that not all analyses have both U and trace element*
505 *(TE) data, therefore there are fewer grains represented in this scatter plot than in Figure 7.*

506



507

508 *Figure 9. Uncorrected rutile U-Pb results in Tera-Wasserburg space colored by Zr-in-rutile temperature calculated from the*
 509 *Kohn (2020) calibration. The mode centered around 95 Ma has the highest temperatures, and modes centered around 300 Ma*
 510 *and 500–650 Ma also contain high temperatures, whereas the 185 Ma mode is predominantly composed of moderate*
 511 *temperature grains. Open circles are rutile U-Pb analyses without trace element (TE) data. Colormap is from Crameri (2020).*

512 **7 Discussion**

513 **7.1 Recommendations for U-Pb Data Rejection, Correction, and Filtering**

514 The complex, natural dataset presented here allows an examination of the current practices of data reporting and
 515 limitations of large-*n* detrital rutile studies. In this study, a large number of analyses were rejected during U-Pb data reduction,
 516 but the SEM images do not provide simple criteria (e.g., inclusions, fractures) for how to better select grains that will produce
 517 acceptable signal quality or lower U-Pb discordance (Figure 2). All areas selected for analysis appeared inclusion-free before
 518 ablation, yet some analyses evidently ablated into inclusions (Figure 2b,e). Because we expected grains from mafic sources
 519 with low U or low Pb concentrations, we used a large 50 μm laser beam diameter, but this potentially increased the probability
 520 of hitting inclusions. While rejecting analyses is not ideal, low U and Pb signal intensities are not unexpected in natural
 521 samples, so some degree of data rejection is to be anticipated, especially given the predicted metamafic (very low U) protolith
 522 sources. We contend here that the exclusion of data from interpretation is common to many detrital rutile studies (e.g., Bracciali
 523 et al., 2013; Rösel et al., 2014, 2019; Caracciolo et al., 2021), ours included. However, in most studies, the number of discarded
 524 analyses and criteria for discarding analyses during U-Pb data reduction are unclear or not mentioned, thereby limiting
 525 opportunities to evaluate data quality and navigate results in a potentially meaningful way. We recommend that these criteria
 526 be explicitly stated and discussed in all studies using detrital rutile U-Pb geochronology.

527 We reiterate that the number of discarded analyses is surprising but is the result of a natural dataset and not analytical
 528 or data reduction error. Daily instrument tuning on NIST 612 glass produced stable signal, high count rates and low oxide
 529 production (Table S2), therefore, the grains rejected due to “spiky” raw signal intensity are not a sign of poor instrument set-

530 up. Further, a comparison of U-Pb precision between our results and other rutile U-Pb studies (Figure S12; Jenkins et al., 2023;
531 Bracciali et al., 2015; Odlum et al., 2024) demonstrates that, for rutile with U concentrations in the parts per million range (>
532 1 ppm U), we achieve lower uncertainty compared with unknowns analyzed on a multi-collector and similar precision for
533 reference materials analyzed on a Q-ICP-MS. Additionally, this study's rutile range extends to 100 times or lower uranium
534 concentration than rutile analyzed by other instrument set-ups. Rutile with high uncertainty in this study is in the lower U range
535 (< 1 ppm U).

536 The uncorrected U-Pb results include many discordant analyses (Figure 3). If treated similar to detrital zircon datasets,
537 many analyses would be excluded by a discordance filter. However, including initially discordant data is acceptable because
538 geologically meaningful interpretations can be made from initially discordant data when appropriate common Pb corrections
539 are applied. U-Pb discordance in common Pb bearing minerals is well documented in published reference materials (e.g., Chew
540 et al., 2011, 2014). In petrochronologic applications, *in-situ* work demonstrates that individual analyses can be nearly 100%
541 discordant and still interpreted confidently within the population of co-genetic grains (e.g., Poulaki et al., 2023). Although
542 some detrital rutile U-Pb datasets are dominated by concordant analyses (e.g., Rösel et al., 2019, Kooijman et al. 2010), many
543 detrital datasets contain analyses across the concordance spectrum, including highly discordant analyses, whose Pb-corrected
544 dates are used in interpretations (Bracciali et al., 2013; Mark et al., 2016; O'Sullivan et al., 2016; Govin et al., 2018; Ershova
545 et al., 2024). Note that common ^{208}Pb and ^{207}Pb corrections force concordance so that initially discordant data are concordant
546 after correction. We propose that the Stacey-Kramers distance is a suitable metric for quantifying discordance as it reflects U-
547 Pb systematics (Figure S8). However, a discordance threshold is not recommended as an exclusion criterion based on the
548 similarity of the date distributions across concordance bins (Figure 6). Further, most mafic-classified grains plot closer to
549 common Pb compositions, so a discordance filter would bias results toward pelitic and high U grains (Figure 7). For these
550 reasons, we do not advocate filtering detrital rutile U-Pb data based on discordance.

551 After U-Pb data reduction, a common Pb correction and uncertainty filter were applied, which further excluded
552 analyses. In this dataset, the ^{208}Pb and ^{207}Pb corrections produce similar date spectra (Figure 4), and either correction method
553 can be used. Similarly, the various uncertainty filters produce similar date distributions (Figure 5) and we tentatively favor the
554 power law uncertainty filter as it does not appear to alter the presence or proportion of individual age populations, and because
555 this filter excludes the fewest analyses. Future work with large-*n* detrital datasets is needed to explore how common Pb
556 corrections, discordance filters, and uncertainty filters influence date distributions in other datasets.

557 Expanding detrital rutile U-Pb applications is hindered by data rejection, as seen in this dataset and others. Caracciolo
558 et al. (2021) attempted to present a large-*n* detrital rutile dataset in which rutile grains were identified via Raman spectroscopy.
559 Their workflow using automated Raman is better suited for identifying polymorphs and reducing bias than the handpicking
560 and SEM-EDS workflow used here and in many other studies. However, of the 712 detrital rutile grains analyzed by Caracciolo
561 et al. (2021), only 347 grains remained (48%) after their data reduction and uncertainty filtering (using a modified power law
562 filter). Similar to our dataset, there were not enough rutile dates per sample to discuss sample-by-sample provenance
563 interpretations (Figure S7). Govin et al. (2018) discarded 36% ($n=53/146$) of detrital rutile U-Pb analyses using their date-

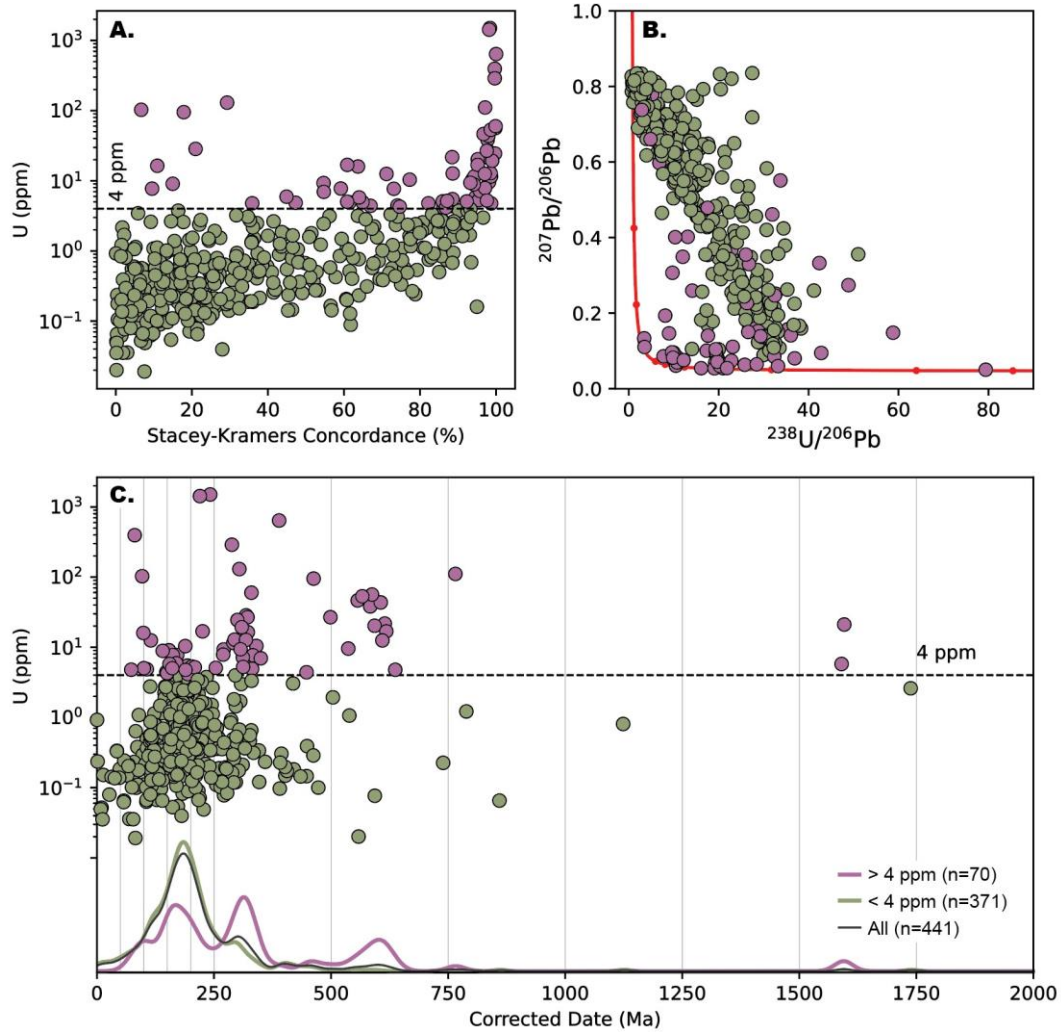
564 dependent filter. Shaanan et al. (2020) present the only other detrital rutile dataset from Anatolia that does not impose a low-
565 U filter; they discard 60% (n=97/163) of their data during discordance filtering. Together these studies illustrate that there is a
566 formidable hurdle in trying to scale up detrital rutile U-Pb to large-*n* provenance applications.

567 **7.2 Low Uranium Rutile**

568 Rejecting and filtering data is a common practice, whether due to abnormal signal intensity pattern, discordance, or
569 high uncertainty. A filter based on the raw data (i.e., low U CPS) is directly linked to counting statistics, which is a fundamental
570 statistical limitation and not instrument type or instrument setting specific. Figure S12 shows that the main issue with the
571 dataset presented here is the very low U and therefore Pb concentration. We demonstrate that the very, very low concentration
572 grains have corresponding low counts and therefore high uncertainty, and are therefore rejected. The rutile in this study has
573 significantly lower U concentrations than many other studies (Figure S12). There is a good reason to reject data with high
574 uncertainty, because they do not allow geologically significant dates to be calculated. In contrast, using a filter based on
575 element abundance (i.e., the 4-5 ppm U threshold used in some publications) is dependent on abundance sensitivity (cps/ppm),
576 which depends on the instrument (laser and ICP-MS type) and instrument settings. Isotopic and elemental concentrations are
577 calculated based on the measured count rate (i.e., counts per second, CPS), which is inherently dependent on the individual
578 mass spectrometer and laser ablation parameters (e.g., spot size, fluence). For instruments with lower sensitivity (lower CPS
579 per ppm), the same calculated concentration (i.e., 4-5 ppm) yields lower CPS and therefore higher analytical uncertainties than
580 for instruments with higher sensitivity. In this way, the U threshold filter based on a calculated concentration is instrument and
581 parameter dependent and we therefore do not recommend this approach of screening rutile to exclude low U concentration
582 analyses.

583 Most studies no longer impose a U threshold, yet, it is a regional concern in Türkiye where two of the four detrital
584 rutile U-Pb datasets only analyze U-Pb on detrital rutile with uranium concentrations above 4-5 ppm (Okay et al., 2011;
585 Şengün et al., 2020). The two studies that do not use a U filter analyze all detrital rutile grains (Shaanan et al., 2020; this
586 study). In this dataset of this study, 87% of detrital rutile are below 4 ppm U (n=537/612). The majority of detrital rutile with
587 $U > 4$ ppm are classified as pelitic and generally have higher Zr contents (higher temperature), whereas low-U rutile in this
588 study generally correlates with lower Zr contents (lower temperature) and includes the majority of mafic-classified grains
589 (Figure 7). Note that there are limitations to the Zr-in-rutile thermometer in mafic rocks if the equilibrium conditions are not
590 met. Figure 10 compares U concentration with concordance and U-Pb date. Concordance does not appear to be correlated
591 with U concentration (Figure 10a). Comparing the date distribution for all grains with that of the groups of grains below and
592 above 4 ppm U reveals that provenance results would be biased by excluding grains below 4 ppm U (Figure 10c). The above
593 4 ppm U group has age modes at 100 Ma, 165 Ma, 315 Ma, 458 Ma, and 600 Ma (Figure 10c pink) whereas the total date
594 spectrum has peaks at 185 Ma, 300 Ma, 400 Ma, 450 Ma and 600 Ma (Figure 10c gray). The above 4 ppm U rutile group has
595 higher amplitude Paleozoic peaks, a minor 100 Ma peak, and a younger, lower amplitude Mesozoic peak (165 Ma vs 185
596 Ma). In summary, the U threshold filter introduces bias into the provenance results because omitting low-U rutile biases

597 results toward metapelitic sources, higher Zr-in-rutile temperatures, and shifts the prominent date modes and their
 598 amplitudes.



599
 600 *Figure 10. Comparison of detrital rutile filtering based on U concentration or concordance. (A) Rutile U concentration versus*
 601 *percent concordance (Stacey-Kramers distance). The U-threshold filter groups grains greater than and less than 4 ppm U. (B)*
 602 *Rutile U-Pb results in Tera-Wasserburg space following the color scheme in panel A. (C) Rutile U concentration versus ²⁰⁷Pb-*
 603 *corrected U-Pb date. The relative KDEs display the date spectra from the different U concentration groups: all analyses,*
 604 *above 4 ppm U, below 4 ppm U. The power law filter is applied to all plots in the figure.*

605

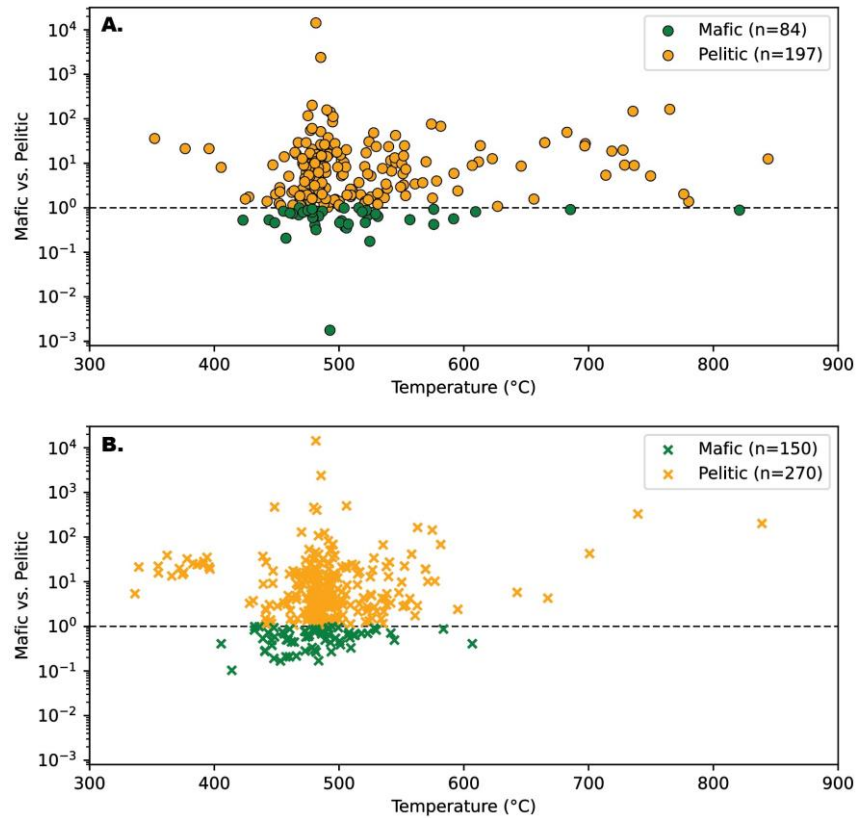
606 7.3 Source Protolith and Metamorphism

607 The Zr-in-rutile thermometer generally preserves the crystallization or recrystallization temperature. The Zr-in-rutile
 608 thermometer can become uncoupled from the U-Pb age because Pb diffusion during medium- to high-temperature

609 metamorphic events or extended cooling periods will cause partial or complete resetting of the U-Pb system (Cherniak et al.,
610 2007; Luvizotto and Zack, 2009; Kooijman et al., 2012; Pereira and Storey, 2023). Because temperatures calculated for the
611 185 Ma population are cooler than for the older events and are not high enough to have reset the U-Pb dates, we interpret these
612 temperatures as primary. Furthermore, partially reset dates would smear the data along concordia from the initial crystallization
613 event age, not towards common Pb. The Zr-in-rutile temperatures and protolith classification are discussed in Section 8 in the
614 context of regional provenance.

615 **7.4 Evaluating Bias in Discarded U-Pb Data**

616 To evaluate the potential bias in U-Pb data reduction and processing, the detrital rutile grains with both U-Pb and
617 trace element data are compared to those with only trace element data (U-Pb rejected and/or excluded by filter). Figure 11
618 gives a sense for what data are missing from the U-Pb results as well as the effects of the uncertainty filter. Note that not all
619 detrital rutile grains have trace element data, so the subset of grains with U-Pb analyses and without trace element data cannot
620 be considered. In the plots of protolith versus Zr-in-rutile temperature, grains included by the power law filter (Figure 11a) are
621 compared to those excluded by the power law filter or without U-Pb data (Figure 11b). Effectively this compares accepted U-
622 Pb analyses to those rejected from unacceptable U-Pb signal patterns or high uncertainties. About 30% of mafic-classified
623 grains and 35% of pelitic-classified grains are acceptable U-Pb analyses included by the power law filter (Figure 11c). The
624 analyses rejected by power law filtering (Figure 11c) have a similar temperature distribution, with the majority of temperatures
625 from 450–550 °C. Most grains with these temperatures fall within the 185 Ma date mode (Figure 9), potentially suggesting
626 that the detrital rutile grains with poor U-Pb precision would have ~185 Ma dates. Further, the rejected analyses group has
627 fewer high temperature pelitic grains (> 600 °C) and a more abundant lower temperature pelitic population (< 400 °C). These
628 temperature windows do not seem diagnostic of specific date populations among pelitic grains, however, about 30% of high
629 temperature pelitic grains fall within the 500-650 Ma population (Figure 9). The similarity in temperature distributions of
630 pelitic and mafic grains between the accepted and rejected U-Pb analyses suggests that there is not significant bias in the U-
631 Pb results due to data rejection. Consequently, we suggest that the U-Pb and trace element data can be used together to
632 interrogate potential bias in U-Pb data rejection and filtering.



633

634 *Figure 11. (A) Protolith versus Zr-in-rutile temperature plot displays all detrital rutile analyses with trace element data*
 635 *included in the power law filter. (B) Plot B shows both the detrital rutile analyses without U-Pb data and those excluded by*
 636 *the power law filter in A. The y-axis values are the transformed distance from the mafic-pelitic discrimination line of Triebold*
 637 *et al. (2012) (Figure 7).*

638 **8 Anatolian Sedimentary Provenance**

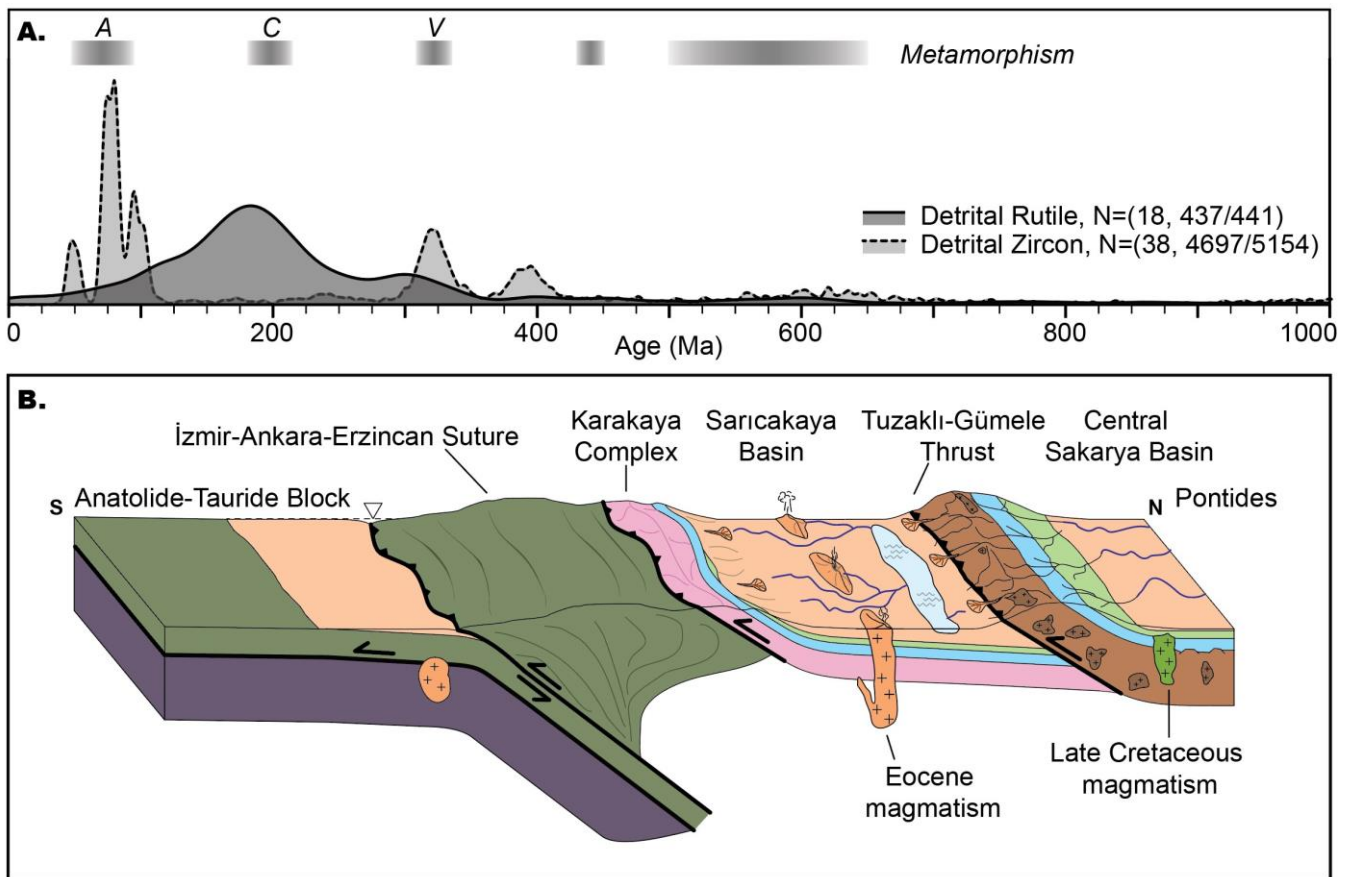
639 Sedimentary provenance is interpreted from all detrital rutile dates together, rather than by sample, due to the small
 640 number of analyses in each sample (see Figure S7 for individual sample results). The detrital rutile results are displayed along
 641 with detrital zircon dates from the same Upper Cretaceous to Eocene units in the Central Sakarya and Sarıcakaya Basins
 642 (Figure 12; data from Campbell, 2017; Ocakoğlu et al., 2018; Mueller et al., 2019, 2022; Okay and Kylander-Clark, 2022).
 643 The detrital zircon and rutile provenance results are discussed together from youngest to oldest date population. The rutile
 644 grains that (poorly) define the ca. 90 Ma population (Figure 12) include some of the highest Zr-in-rutile temperatures (Figure
 645 9). The zircon record has abundant Late Cretaceous and Eocene populations (Figure 12) associated with magmatic flare-ups
 646 during Alpine orogeny-related subduction and syn-collisional magmatism, respectively (Harris et al., 1994; Kasapoğlu et al.,
 647 2016; Yildiz et al., 2015; Ocakoğlu et al., 2018; Mueller et al., 2022; Campbell et al., 2023). The lower plate Anatolide-Tauride
 648 terrane underwent HP/LT blueschist facies metamorphism that generally youngs from Late Cretaceous in the north to early

649 Eocene in the south (Sherlock et al., 1999; Okay and Kelley, 1994; Candan et al., 2005; Pourteau et al., 2016). However, the
650 samples are from sedimentary basins on the Pontides (Figure 12) and the detrital zircon record indicates no sediment transport
651 across the suture zone between from the Anatolide-Tauride terranes to the Pontides in the latest Cretaceous (Okay and
652 Kylander-Clark, 2022). Thus, we interpret the 90 Ma rutile population as either igneous or metamorphic rutile derived from
653 Late Cretaceous magmatism and associated contact metamorphism on the Pontides.

654 The 185 Ma peak includes the lowest Zr-in-rutile temperatures (~450–550 °C; Figure 9), mafic and pelitic sources
655 (Figure 7), and predominantly low U rutile (Figure 10). The age, lithology, and temperature findings support a Karakaya
656 Complex sediment source. The Permian–Triassic Karakaya Complex contains intra-oceanic basalts and forearc deposits that
657 were metamorphosed to blueschist and epidote-amphibolite facies (340–550 ± 50 °C; Okay et al., 2002; Federici et al., 2010)
658 during the Triassic Cimmerian event. The rutile U-Pb dates interpreted as Karakaya Complex (broad 185 Ma peak) are younger
659 than existing Karakaya Complex phengite, glaucophane, and barroisite Ar-Ar cooling dates (~200–215 Ma; Okay et al., 2002;
660 Federici et al., 2010; Şengör et al., 1984). The closure temperature windows for rutile U-Pb and phengite Ar-Ar overlap, with
661 Pb in rutile extending to lower temperature than Ar in phengitic white mica (Itaya, 2020; M. Grove, pers. comm., 2024). The
662 younger rutile dates likely indicate protracted cooling because extended time spent in the partial retention zone would cause
663 variable Pb loss that could lead to a younger rutile U-Pb dates than any actual heating event and/or a spread in ages (broad
664 peak). This 185 Ma population is not prominent in the detrital zircon spectra. Detrital zircons from Karakaya Complex units
665 have age modes at ca. 235 Ma, 315 Ma, and 400 Ma and are interpreted as sediment input to the forearc from the Pontides
666 Triassic magmatic arc, oceanic plateau, or spreading center (e.g., Okay et al., 2015), Variscan granitoids, and crystalline
667 basement (Ustaömer et al., 2016).

668 The Carboniferous peaks in the zircon and rutile record correspond to a ~330–340 Ma pulse of high-T metamorphism
669 and ~290–320 Ma magmatism in the Pontides during the Variscan orogeny (Topuz et al., 2007, 2020; Ustaömer et al., 2012,
670 2013). Variscan-aged detrital rutiles were found in Jurassic sandstones in the Central Sakaraya Basin and interpreted as derived
671 from either primary Pontide basement or recycled sedimentary sources (Şengün et al., 2020). The Pontide basement units crop
672 out along the Tuzaklı-Gümele Thrust fault that partitions the two sedimentary basins (Figure 12b). Therefore, the Variscan-
673 aged detrital rutile could be derived from primary basement sources or recycled Jurassic sedimentary units. The Pontides
674 crystalline basement contains scarce Devonian (380–400 Ma) and Silurian (420–440 Ma) metaigneous rocks, which are
675 exposed in the hanging wall of the Tuzaklı-Gümele Thrust (Topuz et al., 2020). The paucity of this age population in the rutile
676 record could be due to the scarcity of outcrops, small sample size, dilution during sediment recycling, or overprinting by the
677 Carboniferous high temperature event. Late Ordovician–Early Silurian metamorphism associated with the accretion of the
678 Istanbul–Moesia–Scythian Platform (Okay et al., 2006) is not prominent in the detrital rutile record, which could suggest the
679 absence of major south-directed sediment transport across the Pontides (i.e., from the Istanbul Zone to Sakarya Zone across
680 Intra-Pontide ocean/suture) during the Late Cretaceous to Eocene. Lastly, the 500–650 Ma Pan-African detrital rutile ages
681 align with the detrital zircon age spectra. Gondwana-derived terranes are characterized by Neoproterozoic–Cambrian
682 plutonism and metamorphism from the Pan-African–Cadomian orogeny, which is not well documented in Anatolia (Okay et

683 al., 2006). Grains of this age could be sourced from the Pontides basement or recycled from sedimentary units (Ustaömer et
 684 al., 2012; Mueller et al., 2019). However, if the grains of this age were first-cycle from crystalline basement sources, we would
 685 expect them to have reset, younger U-Pb dates reflective of younger metamorphic reheating events. However, by this
 686 reasoning, the presence of 500–650 Ma dates indicates that these grains must have been unaffected by the younger high-T
 687 events (i.e., Variscan, Cimmerian and Alpine metamorphism). In order to have escaped metamorphic reheating, the grains had
 688 to have been already eroded from the crystalline basement and deposited in sedimentary units. Therefore, we interpret the 500–
 689 650 Ma grains as polycyclic grains derived from recycled sedimentary units. Together, the detrital zircon and rutile age spectra
 690 demonstrate that, from the Late Cretaceous to Eocene, sediment was routed to the Central Sakarya and Sarıcakaya Basins from
 691 syn-depositional magmatic centers, the Karakaya Complex within the suture zone, the Pontides crystalline basement, and
 692 recycled sedimentary units (Figure 12).
 693



694

695 *Figure 12. (A) Kernel density estimate of all detrital rutile dates (^{207}Pb -corrected, power law uncertainty filtered) shown*
 696 *alongside a compilation of all published detrital zircon ages from Upper Cretaceous to Eocene strata in Central Sakarya and*
 697 *Sarıcakaya Basins. Gray bars depict periods of metamorphism in western Anatolia. (B) Schematic reconstruction of*
 698 *northwestern Anatolia in the Eocene during continental collision (after Mueller et al., 2019). The main sources of sediment to*

699 *the basins were the Karakaya Complex exposed in the suture zone, Pontides crystalline basement exposed along the Tuzaklı-*
700 *Gümele Thrust, Cretaceous-Eocene igneous units, and recycled sedimentary units. A: Alpine metamorphism, C: Cimmerian*
701 *metamorphism, V: Variscan metamorphism.*

702 **9 Conclusions**

703 This work provides a systematic exploration of the data reduction and processing workflows for detrital rutile U-Pb
704 geochronology using a new dataset from the Central Sakarya and Sarıcakaya Basins in Anatolia. Provenance interpretations
705 are made from combining U-Pb dates and trace element geochemistry. The results have several implications for navigating
706 workflows and interpretations in common Pb bearing detrital minerals:

707 (1) Natural datasets can be complex. While attempting a large-*n* provenance study, a significant number of analyses
708 were discarded due to unacceptable U-Pb signal intensity and stability, namely low U, low Pb, and inclusions. This hurdle is
709 evidently not unique to this dataset and should always be reported in detrital rutile U-Pb geochronology. Advances are needed
710 to determine the best path forward, such as analyzing more grains for achieving large-*n* detrital rutile U-Pb datasets and more
711 rigorous data reporting and standardizing metrics used for evaluating ‘acceptable’ U-Pb analyses. We recommend that the
712 criteria for data rejection be explicitly discussed in all detrital rutile studies.

713 (2) We provide a method for evaluating the potential bias in U-Pb data rejection and filtering by comparing the detrital
714 rutile grains with both U-Pb and trace element data to those with only trace element data. The rejected and filtered out grains
715 have a similar trace element distribution in terms of Zr-in-rutile temperature and mafic-pelitic classification to those with
716 acceptable U-Pb analyses, suggesting there is not significant bias from U-Pb data rejection and filtering.

717 (3) The ²⁰⁸Pb and ²⁰⁷Pb correction methods produce similar age spectra and do not change the final provenance
718 interpretations. Similarly, the uncertainty filters—based on U-Pb ratio uncertainty and corrected date uncertainty—produce
719 similar date spectra. The power law uncertainty filter is preferred because it does not alter the date distribution and includes
720 the most grains.

721 (4) There has not been an agreed upon metric to quantify discordance in common Pb minerals. We evaluate various
722 distance metrics (Text S3) and recommend the Stacey-Kramers distance as a suitable metric for quantifying discordance.
723 However, because reliable interpretations can be made from analyses with significant proportions of common Pb, we do not
724 recommend applying a discordance filter to common Pb detrital minerals.

725 (5) In some labs and geographic locations, only rutile above a certain uranium concentration (i.e., 4-5 ppm U) are
726 analyzed for U-Pb. We demonstrate that excluding low-U rutile biases provenance interpretations toward grains with pelitic
727 protoliths, higher Zr-in-rutile temperatures, and higher concordance, and changes the overall date distribution, especially the
728 amplitude of date peaks.

729 (6) A significant challenge in provenance work is pinpointing the signature of sediment recycling. Here we use paired
730 U-Pb dates and Zr-in-rutile temperatures to identify polycyclic detrital rutile grains. The recycled grains preserve U-Pb dates

731 that indicate that they escaped younger metamorphic reheating events of the crystalline basement by already being eroded and
732 deposited in sedimentary units. In this way, detrital rutile petrochronology can address problems of sediment recycling.

733 (7) The data processing workflows used here are provided as code in Jupyter Notebooks that can be used by future
734 studies. The code includes common Pb corrections, uncertainty filters, discordance calculations, and trace element plots. The
735 provided code is one path forward to achieving the required documentation and unification of data reduction approaches.

736 **Data and code availability**

737 All of the data generated in this manuscript are publicly archived and available in an Open Science Framework data
738 repository that can be accessed at <https://doi.org/10.17605/OSF.IO/A4YE5> (Mueller et al., 2023). The data repository also
739 includes the supporting information text. Jupyter Notebooks containing the Python and R code used for data reduction and
740 visualization are open and available at <https://zenodo.org/doi/10.5281/zenodo.10636727> (Mueller, 2024).

741 **Author contributions**

742 MAM conceptualized the project; MAM and AL acquired funding; all authors were involved in the investigation;
743 MAM and AM performed the formal data collection; all authors contributed to writing and revising the manuscript.

744 **Competing interests**

745 The authors declare that they have no conflict of interest.

746 **Disclaimer**

747 The software described here is provided under the Apache License, Version 2.0. It is provided "as is," without
748 warranty of any kind, express or implied, including but not limited to the warranties of merchantability, fitness for a particular
749 purpose, and noninfringement. In no event shall the authors or copyright holders be liable for any claim, damages, or other
750 liability, whether in an action of contract, tort, or otherwise, arising from, out of, or in connection with the software or the use
751 or other dealings in the software.

752 **Acknowledgements**

753 We thank Çelik Ocakoğlu, Jan Westerweel, Kate Huntington, Alison Duvall, Scott Braswell, Joel DesOrmeau, Sean
754 Mulcahy, Scott Dakins, and Eric Steig for support in the field and lab. We thank Andrew Kylander-Clark, Francisco Apen,
755 and Peter Downes for reference materials and Stuart Thomson, Margo Odlum, Eirini Poulaki, and Drew Levy for discussions

756 on common Pb corrections. We thank the iolite team for student access. We thank Associate Editor Pieter Vermeesch and
757 referees David Chew, Laura Bracciali, Ines Pereira and an anonymous reviewer for thoughtful reviews that improved the
758 manuscript.

759 **Financial support**

760 This work was funded by the University of Washington Department of Earth and Space Sciences and NSF EAR-
761 1543684 and EAR-2141115.

762 **References**

763 Açıkalın, S., Ocakoğlu, F., Yılmaz, İ. Ö., Vonhof, H., Hakyemez, A., and Smit, J.: Stable isotopes and geochemistry of a
764 Campanian–Maastrichtian pelagic succession, Mudurnu–Göynük Basin, NW Turkey: Implications for palaeoceanography,
765 palaeoclimate and sea-level fluctuations, *Palaeogeogr. Palaeoclimatol. Palaeoecol.*, 441, 453–466,
766 <https://doi.org/10.1016/j.palaeo.2015.10.005>, 2016.

767 Aksay, A., Pehlivan, Ş., Gedik, I., Bilginer, E., Duru, M., Akbaş, B., and Altun, I.: Geologic map of Turkey (Zonguldak, Scale
768 1:500,000), Maden Tetkik ve Arma Genel Müdürlüğü, Ankara, Turkey, 2002.

769 Andersen, T.: Correction of common lead in U–Pb analyses that do not report ^{204}Pb , *Chem. Geol.*, 192, 59–79,
770 [https://doi.org/10.1016/S0009-2541\(02\)00195-X](https://doi.org/10.1016/S0009-2541(02)00195-X), 2002.

771 Angiboust, S. and Harlov, D.: Ilmenite breakdown and rutile-titanite stability in metagranitoids: Natural observations and
772 experimental results, *Am. Mineral.*, 102, 1696–1708, <https://doi.org/10.2138/am-2017-6064>, 2017.

773 Apen, F. E., Rudnick, R. L., Cottle, J. M., Kylander-Clark, A. R. C., Blondes, M. S., Piccoli, P. M., and Seward, G.: Four-
774 dimensional thermal evolution of the East African Orogen: accessory phase petrochronology of crustal profiles through the
775 Tanzanian Craton and Mozambique Belt, northeastern Tanzania, *Contrib. Mineral. Petrol.*, 175, 97,
776 <https://doi.org/10.1007/s00410-020-01737-6>, 2020.

777 Blackburn, T. J., Bowring, S. A., Perron, J. T., Mahan, K. H., Dudas, F. O., and Barnhart, K. R.: An Exhumation History of
778 Continents over Billion-Year Time Scales, *Science*, 335, 73–76, <https://doi.org/10.1126/science.1213496>, 2012.

779 Blum, M. and Pecha, M.: Mid-Cretaceous to Paleocene North American drainage reorganization from detrital zircons,
780 *Geology*, 42, 607–610, <https://doi.org/10.1130/G35513.1>, 2014.

781 Bracciali, L.: Coupled Zircon-Rutile U-Pb Chronology: LA ICP-MS Dating, Geological Significance and Applications to
782 Sediment Provenance in the Eastern Himalayan-Indo-Burman Region, *Geosciences*, 9, 467,
783 <https://doi.org/10.3390/geosciences9110467>, 2019.

784 Bracciali, L., Parrish, R. R., Horstwood, M. S. A., Condon, D. J., and Najman, Y.: UPb LA-(MC)-ICP-MS dating of rutile:
785 New reference materials and applications to sedimentary provenance, *Chem. Geol.*, 347, 82–101,
786 <https://doi.org/10.1016/j.chemgeo.2013.03.013>, 2013.

- 787 Bracciali, L., Najman, Y., Parrish, R. R., Akhter, S. H., and Millar, I.: The Brahmaputra tale of tectonics and erosion: Early
788 Miocene river capture in the Eastern Himalaya, *Earth Planet. Sci. Lett.*, 415, 25–37, <https://doi.org/10.1016/j.epsl.2015.01.022>,
789 2015.
- 790 Campbell, C. F.: Tectonic Evolution of the Izmir-Ankara Suture Zone in Northwest Turkey using Zircon U-Pb Geochronology
791 and Zircon Lu-Hf Isotopic Tracers, M.S., University of Kansas, United States -- Kansas, 99 pp., 2017.
- 792 Campbell, C. F., Mueller, M. A., Taylor, M. H., Oçakoğlu, F., Möller, A., Métais, G., Coster, P. M. C., Beard, K. C., and Licht,
793 A.: The Geodynamic Implications of Passive Margin Subduction in Northwest Turkey, *Geochem. Geophys. Geosystems*, 24,
794 e2022GC010481, <https://doi.org/10.1029/2022GC010481>, 2023.
- 795 Candan, O., Çetinkaplan, M., Oberhänsli, R., Rimmelé, G., and Akal, C.: Alpine high-P/low-T metamorphism of the Afyon
796 Zone and implications for the metamorphic evolution of Western Anatolia, Turkey, *Lithos*, 84, 102–124,
797 <https://doi.org/10.1016/j.lithos.2005.02.005>, 2005.
- 798 Caracciolo, L., Ravidà, D. C. G., Chew, D., Janßen, M., Lünsdorf, N. K., Heins, W. A., Stephan, T., and Stollhofen, H.:
799 Reconstructing environmental signals across the Permian-Triassic boundary in the SE Germanic Basin: A Quantitative
800 Provenance Analysis (QPA) approach, *Glob. Planet. Change*, 206, 103631, <https://doi.org/10.1016/j.gloplacha.2021.103631>,
801 2021.
- 802 Carrapa, B.: Resolving tectonic problems by dating detrital minerals, *Geology*, 38, 191–192,
803 <https://doi.org/10.1130/focus022010.1>, 2010.
- 804 Cave, B. J., Stepanov, A. S., Craw, D., Large, R. R., Halpin, J. A., and Thompson, J.: RELEASE OF TRACE ELEMENTS
805 THROUGH THE SUB-GREENSCHIST FACIES BREAKDOWN OF DETRITAL RUTILE TO METAMORPHIC
806 TITANITE IN THE OTAGO SCHIST, NEW ZEALAND, *Can. Mineral.*, 53, 379–400,
807 <https://doi.org/10.3749/canmin.1400097>, 2015.
- 808 Cherniak, D. J.: Pb diffusion in rutile, *Contrib. Mineral. Petrol.*, 139, 198–207, <https://doi.org/10.1007/PL00007671>, 2000.
- 809 Cherniak, D. J., Manchester, J., and Watson, E. B.: Zr and Hf diffusion in rutile, *Earth Planet. Sci. Lett.*, 261, 267–279,
810 <https://doi.org/10.1016/j.epsl.2007.06.027>, 2007.
- 811 Chew, D., O’Sullivan, G., Caracciolo, L., Mark, C., and Tyrrell, S.: Sourcing the sand: Accessory mineral fertility, analytical
812 and other biases in detrital U-Pb provenance analysis, *Earth-Sci. Rev.*, 202, 103093,
813 <https://doi.org/10.1016/j.earscirev.2020.103093>, 2020.
- 814 Chew, D. M., Sylvester, P. J., and Tubrett, M. N.: U–Pb and Th–Pb dating of apatite by LA-ICPMS, *Chem. Geol.*, 280, 200–
815 216, <https://doi.org/10.1016/j.chemgeo.2010.11.010>, 2011.
- 816 Chew, D. M., Petrus, J. A., and Kamber, B. S.: U-Pb LA-ICPMS dating using accessory mineral standards with variable
817 common Pb, *Chem. Geol.*, 363, 185–199, <https://doi.org/10.1016/j.chemgeo.2013.11.006>, 2014.
- 818 Clark, D. J., Hensen, B. J., and Kinny, P. D.: Geochronological constraints for a two-stage history of the Albany–Fraser
819 Orogen, Western Australia, *Precambrian Res.*, 102, 155–183, [https://doi.org/10.1016/S0301-9268\(00\)00063-2](https://doi.org/10.1016/S0301-9268(00)00063-2), 2000.
- 820 Clift, P. D., Hodges, K. V., Heslop, D., Hannigan, R., Van Long, H., and Calves, G.: Correlation of Himalayan exhumation
821 rates and Asian monsoon intensity, *Nat. Geosci.*, 1, 875–880, <https://doi.org/10.1038/ngeo351>, 2008.

- 822 Clift, P. D., Mark, C., Alizai, A., Khan, H., and Jan, M. Q.: Detrital U–Pb rutile and zircon data show Indus River sediment
823 dominantly eroded from East Karakoram, not Nanga Parbat, *Earth Planet. Sci. Lett.*, 600, 117873,
824 <https://doi.org/10.1016/j.epsl.2022.117873>, 2022.
- 825 Compston, W., Williams, I. S., and Meyer, C.: U-Pb geochronology of zircons from lunar breccia 73217 using a sensitive high
826 mass-resolution ion microprobe, *J. Geophys. Res. Solid Earth*, 89, B525–B534, <https://doi.org/10.1029/JB089iS02p0B525>,
827 1984.
- 828 Crameri, F., Shephard, G. E., and Heron, P. J.: The misuse of colour in science communication, *Nat. Commun.*, 11, 5444,
829 <https://doi.org/10.1038/s41467-020-19160-7>, 2020.
- 830 Davis, W. J., Canil, D., MacKenzie, J. M., and Carbone, G. B.: Petrology and U–Pb geochronology of lower crustal xenoliths
831 and the development of a craton, Slave Province, Canada, *Lithos*, 71, 541–573, [https://doi.org/10.1016/S0024-4937\(03\)00130-](https://doi.org/10.1016/S0024-4937(03)00130-0)
832 0, 2003.
- 833 Dickinson, W. R. and Suczek, C. A.: Plate Tectonics and Sandstone Compositions, *AAPG Bull.*, 63, 2164–2182, 1979.
- 834 Dodson, M. H.: Closure Temperature in Cooling Geochronological and Petrological Systems, *Contrib. Mineral. Petrol.*, 40,
835 259–274, 1973.
- 836 Ershova, V., Prokopyev, A., and Stockli, D.: Provenance of Detrital Rutiles from the Triassic–Jurassic Sandstones in Franz
837 Josef Land (Barents Sea Region, Russian High Arctic): U-Pb Ages and Trace Element Geochemistry, *Geosciences*, 14, 41,
838 <https://doi.org/10.3390/geosciences14020041>, 2024.
- 839 Ersoy, E. Y., Akal, C., Genç, Ş. C., Candan, O., Palmer, M. R., Prelević, D., Uysal, İ., and Mertz-Kraus, R.: U-Pb zircon
840 geochronology of the Paleogene – Neogene volcanism in the NW Anatolia: Its implications for the Late Mesozoic-Cenozoic
841 geodynamic evolution of the Aegean, *Tectonophysics*, 717, 284–301, <https://doi.org/10.1016/j.tecto.2017.08.016>, 2017.
- 842 Ersoy, E. Y., Akal, C., Palmer, M. R., and Mertz-Kraus, R.: U-Pb dating of arc to post-collisional magmatic events in
843 northwestern Anatolia: The Eocene Granitoids in NW Anatolia revisited, *J. Asian Earth Sci.* X, 9, 100148,
844 <https://doi.org/10.1016/j.jaesx.2023.100148>, 2023.
- 845 Ewing, T. A.: Hf isotope analysis and U-Pb geochronology of rutile : technique development and application to a lower crustal
846 section (Ivrea-Verbano Zone, Italy), <https://doi.org/10.25911/5d74e68841e8d>, 2011.
- 847 Ewing, T. A., Rubatto, D., Beltrando, M., and Hermann, J.: Constraints on the thermal evolution of the Adriatic margin during
848 Jurassic continental break-up: U–Pb dating of rutile from the Ivrea–Verbano Zone, Italy, *Contrib. Mineral. Petrol.*, 169, 44,
849 <https://doi.org/10.1007/s00410-015-1135-6>, 2015.
- 850 Faure, G.: *Principles of Isotope Geology*, 2nd Edition., Wiley & Sons, Inc., 608 pp., 1986.
- 851 Federici, I., CAVAZZA, W., OKAY, A. I., BEYSSAC, O., ZATTIN, M., CORRADO, S., and DELLISANTI, F.: Thermal
852 Evolution of the Permo–Triassic Karakaya Subduction-accretion Complex between the Biga Peninsula and the Tokat Massif
853 (Anatolia), *Turk. J. Earth Sci.*, 19, 409–429, <https://doi.org/10.3906/yer-0910-39>, 2010.
- 854 Ferry, J. M. and Watson, E. B.: New thermodynamic models and revised calibrations for the Ti-in-zircon and Zr-in-rutile
855 thermometers, *Contrib. Mineral. Petrol.*, 154, 429–437, <https://doi.org/10.1007/s00410-007-0201-0>, 2007.
- 856 Flowers, R. M., Bowring, S. A., Tulloch, A. J., and Klepeis, K. A.: Tempo of burial and exhumation within the deep roots of
857 a magmatic arc, Fiordland, New Zealand, *Geology*, 33, 17–20, <https://doi.org/10.1130/G21010.1>, 2005.

- 858 Foley, S. F., Barth, M. G., and Jenner, G. A.: Rutile/melt partition coefficients for trace elements and an assessment of the
859 influence of rutile on the trace element characteristics of subduction zone magmas, *Geochim. Cosmochim. Acta*, 64, 933–938,
860 [https://doi.org/10.1016/S0016-7037\(99\)00355-5](https://doi.org/10.1016/S0016-7037(99)00355-5), 2000.
- 861 Garzanti, E. and Andò, S.: Heavy Mineral Concentration in Modern Sands: Implications for Provenance Interpretation, in:
862 *Developments in Sedimentology*, vol. 58, edited by: Mange, M. A. and Wright, D. T., Elsevier, 517–545,
863 [https://doi.org/10.1016/S0070-4571\(07\)58020-9](https://doi.org/10.1016/S0070-4571(07)58020-9), 2007.
- 864 Garzanti, E., Doglioni, C., Vezzoli, G., and Ando, S.: Orogenic belts and orogenic sediment provenance, *J. Geol.*, 115, 315–
865 334, 2007.
- 866 Gaschnig, R. M.: Benefits of a Multiproxy Approach to Detrital Mineral Provenance Analysis: An Example from the
867 Merrimack River, New England, USA, *Geochem. Geophys. Geosystems*, 20, 1557–1573,
868 <https://doi.org/10.1029/2018GC008005>, 2019.
- 869 Gazzi, P.: On the Heavy Mineral Zones in the Geosyncline Series. Recent Studies in the Northern Apennines, Italy, *J.*
870 *Sediment. Petrol.*, 35, 109–115, <https://doi.org/10.1306/74D71203-2B21-11D7-8648000102C1865D>, 1965.
- 871 Gehrels, G.: Detrital Zircon U-Pb Geochronology: Current Methods and New Opportunities, in: *Tectonics of Sedimentary*
872 *Basins*, John Wiley & Sons, Ltd, 45–62, <https://doi.org/10.1002/9781444347166.ch2>, 2011.
- 873 Gehrels, G.: Detrital Zircon U-Pb Geochronology Applied to Tectonics, *Annu. Rev. Earth Planet. Sci.*, 42, 127–149,
874 <https://doi.org/10.1146/annurev-earth-050212-124012>, 2014.
- 875 Gehrels, G. E., Valencia, V. A., and Ruiz, J.: Enhanced precision, accuracy, efficiency, and spatial resolution of U-Pb ages by
876 laser ablation–multicollector–inductively coupled plasma–mass spectrometry, *Geochem. Geophys. Geosystems*, 9, Q03017,
877 <https://doi.org/10.1029/2007GC001805>, 2008.
- 878 Göncüoğlu, M. C., Turhan, N., Şentürk, K., Özcan, A., Uysal, Ş., and Yaliniz, M. K.: A Geotraverse Across Northwestern
879 Turkey: Tectonic Units of the Central Sakarya Region and their Tectonic Evolution, *Geol. Soc. Lond. Spec. Publ.*, 173, 139–
880 161, <https://doi.org/10.1144/GSL.SP.2000.173.01.06>, 2000.
- 881 Govin, G., Najman, Y., Copley, A., Millar, I., van der Beek, P., Huyghe, P., Grujic, D., and Davenport, J.: Timing and
882 mechanism of the rise of the Shillong Plateau in the Himalayan foreland, *Geology*, 46, 279–282,
883 <https://doi.org/10.1130/G39864.1>, 2018.
- 884 Guo, R., Hu, X., Garzanti, E., Lai, W., Yan, B., and Mark, C.: How faithfully do the geochronological and geochemical
885 signatures of detrital zircon, titanite, rutile and monazite record magmatic and metamorphic events? A case study from the
886 Himalaya and Tibet, *Earth-Sci. Rev.*, 201, 103082, <https://doi.org/10.1016/j.earscirev.2020.103082>, 2020.
- 887 Harris, N. B. W., Kelley, S., and Okay, A. I.: Post-collisional magmatism and tectonics in northwest Anatolia, *Contrib. Mineral.*
888 *Petrol.*, 117, 241–252, 1994.
- 889 Hart, E., Storey, C., Bruand, E., Schertl, H.-P., and Alexander, B. D.: Mineral inclusions in rutile: A novel recorder of HP–
890 UHP metamorphism, *Earth Planet. Sci. Lett.*, 446, 137–148, <https://doi.org/10.1016/j.epsl.2016.04.035>, 2016.
- 891 Hart, E., Storey, C., Harley, S. L., and Fowler, M.: A window into the lower crust: Trace element systematics and the
892 occurrence of inclusions/intergrowths in granulite-facies rutile, *Gondwana Res.*, 59, 76–86,
893 <https://doi.org/10.1016/j.gr.2018.02.021>, 2018.

- 894 Hietpas, J., Samson, S., Moecher, D., and Schmitt, A. K.: Recovering tectonic events from the sedimentary record: Detrital
895 monazite plays in high fidelity, *Geology*, 38, 167–170, <https://doi.org/10.1130/G30265.1>, 2010.
- 896 Hietpas, J., Samson, S., Moecher, D., and Chakraborty, S.: Enhancing tectonic and provenance information from detrital zircon
897 studies: assessing terrane-scale sampling and grain-scale characterization, *J. Geol. Soc.*, 168, 309–318,
898 <https://doi.org/10.1144/0016-76492009-163>, 2011.
- 899 Hubert, J. F.: Analysis of heavy-mineral assemblages, in: *Procedures in sedimentary petrology*, edited by: Carver, R. E., New
900 York: Wiley-Interscience, 453–478, 1971.
- 901 Itaya, T.: K–Ar phengite geochronology of HP–UHP metamorphic rocks –An in–depth review–, *J. Mineral. Petrol. Sci.*, 115,
902 44–58, <https://doi.org/10.2465/jmps.190123>, 2020.
- 903 Jenkins, K., Goemann, K., Belousov, I., Morissette, M., and Danyushevsky, L.: Investigation of the Ablation Behaviour of
904 Andradite-Grossular Garnets and Rutile with Implications for U-Pb Geochronology, *Geostand. Geoanalytical Res.*, 47, 267–
905 295, <https://doi.org/10.1111/ggr.12478>, 2023.
- 906 Jochum, K. P., Wilson, S. A., Abouchami, W., Amini, M., Chmeleff, J., Eisenhauer, A., Hegner, E., Iaccheri, L. M., Kieffer,
907 B., Krause, J., McDonough, W. F., Mertz-Kraus, R., Raczek, I., Rudnick, R. L., Scholz, D., Steinhoefel, G., Stoll, B., Stracke,
908 A., Tonarini, S., Weis, D., Weis, U., and Woodhead, J. D.: GSD-1G and MPI-DING Reference Glasses for In Situ and Bulk
909 Isotopic Determination, *Geostand. Geoanalytical Res.*, 35, 193–226, <https://doi.org/10.1111/j.1751-908X.2010.00114.x>, 2011.
- 910 Kasapoğlu, B., Ersoy, Y. E., Uysal, İ., Palmer, M. R., Zack, T., Koralay, E. O., and Karlsson, A.: The petrology of Paleogene
911 volcanism in the Central Sakarya, Nallıhan Region: Implications for the initiation and evolution of post-collisional, slab break-
912 off-related magmatic activity, *Lithos*, 246–247, 81–98, <https://doi.org/10.1016/j.lithos.2015.12.024>, 2016.
- 913 Kellett, D. A., Weller, O. M., Zagorevski, A., and Regis, D.: A petrochronological approach for the detrital record: Tracking
914 mm-sized eclogite clasts in the northern Canadian Cordillera, *Earth Planet. Sci. Lett.*, 494, 23–31,
915 <https://doi.org/10.1016/j.epsl.2018.04.036>, 2018.
- 916 Keskin, M. and Tüysüz, O.: Stratigraphy, petrogenesis and geodynamic setting of Late Cretaceous volcanism on the SW
917 margin of the Black Sea, Turkey, *Geol. Soc. Lond. Spec. Publ.*, 464, 95–130, <https://doi.org/10.1144/SP464.5>, 2018.
- 918 Klemme, S., Blundy, J. D., and Wood, B. J.: Experimental constraints on major and trace element partitioning during partial
919 melting of eclogite, *Geochim. Cosmochim. Acta*, 66, 3109–3123, [https://doi.org/10.1016/S0016-7037\(02\)00859-1](https://doi.org/10.1016/S0016-7037(02)00859-1), 2002.
- 920 Kohn, M. J.: A refined zirconium-in-rutile thermometer, *Am. Mineral.*, 105, 963–971, <https://doi.org/10.2138/am-2020-7091>,
921 2020.
- 922 Kohn, M. J. and Kelly, N. M.: Petrology and Geochronology of Metamorphic Zircon, in: *Geophysical Monograph Series*,
923 edited by: Moser, D. E., Corfu, F., Darling, J. R., Reddy, S. M., and Tait, K., John Wiley & Sons, Inc., Hoboken, NJ, USA,
924 35–61, <https://doi.org/10.1002/9781119227250.ch2>, 2017.
- 925 Kooijman, E., Mezger, K., and Berndt, J.: Constraints on the U–Pb systematics of metamorphic rutile from in situ LA-ICP-
926 MS analysis, *Earth Planet. Sci. Lett.*, 293, 321–330, <https://doi.org/10.1016/j.epsl.2010.02.047>, 2010.
- 927 Kooijman, E., Smit, M. A., Mezger, K., and Berndt, J.: Trace element systematics in granulite facies rutile: implications for
928 Zr geothermometry and provenance studies, *J. Metamorph. Geol.*, 30, 397–412, <https://doi.org/10.1111/j.1525-1314.2012.00972.x>, 2012.

- 930 Kylander-Clark, A. R. C.: Slow subduction and exhumation of a thick ultrahigh -pressure terrane: Western Gneiss Region,
931 Norway, Ph.D., University of California, Santa Barbara, United States -- California, 121 pp., 2008.
- 932 Kylander-Clark, A. R. C., Hacker, B. R., and Mattinson, J. M.: Slow exhumation of UHP terranes: Titanite and rutile ages of
933 the Western Gneiss Region, Norway, *Earth Planet. Sci. Lett.*, 272, 531–540, <https://doi.org/10.1016/j.epsl.2008.05.019>, 2008.
- 934 Lippert, P. G.: Detrital U-Pb geochronology provenance analyses: case studies in the Greater Green River Basin, Wyoming,
935 and the Book Cliffs, Utah, Thesis, University of Kansas, 2014.
- 936 Ludwig, K. R.: On the Treatment of Concordant Uranium-Lead Ages, *Geochim. Cosmochim. Acta*, 62, 665–676,
937 [https://doi.org/10.1016/S0016-7037\(98\)00059-3](https://doi.org/10.1016/S0016-7037(98)00059-3), 1998.
- 938 Luvizotto, G. L. and Zack, T.: Nb and Zr behavior in rutile during high-grade metamorphism and retrogression: An example
939 from the Ivrea–Verbano Zone, *Chem. Geol.*, 261, 303–317, <https://doi.org/10.1016/j.chemgeo.2008.07.023>, 2009.
- 940 Luvizotto, G. L., Zack, T., Meyer, H. P., Ludwig, T., Triebold, S., Kronz, A., Munker, C., Stockli, D. F., Prowatke, S., Klemme,
941 S., Jacob, D. E., and von Eynatten, H.: Rutile crystals as potential trace element and isotope mineral standards for
942 microanalysis, *Chem. Geol.*, 261, 346–369, <https://doi.org/10.1016/j.chemgeo.2008.04.012>, 2009.
- 943 Mark, C., Cogné, N., and Chew, D.: Tracking exhumation and drainage divide migration of the Western Alps: A test of the
944 apatite U-Pb thermochronometer as a detrital provenance tool, *GSA Bull.*, 128, 1439–1460, <https://doi.org/10.1130/B31351.1>,
945 2016.
- 946 McLean, N. M., Bowring, J. F., and Bowring, S. A.: An algorithm for U-Pb isotope dilution data reduction and uncertainty
947 propagation, *Geochem. Geophys. Geosystems*, 12, <https://doi.org/10.1029/2010GC003478>, 2011.
- 948 Meinhold, G.: Rutile and its applications in earth sciences, *Earth-Sci. Rev.*, 102, 1–28,
949 <https://doi.org/10.1016/j.earscirev.2010.06.001>, 2010.
- 950 Meinhold, G., Anders, B., Kostopoulos, D., and Reischmann, T.: Rutile chemistry and thermometry as provenance indicator:
951 An example from Chios Island, Greece, *Sediment. Geol.*, 203, 98–111, <https://doi.org/10.1016/j.sedgeo.2007.11.004>, 2008.
- 952 Meinhold, G., MORTON, A. C., FANNING, C. M., and WHITHAM, A. G.: U–Pb SHRIMP ages of detrital granulite-facies
953 rutiles: further constraints on provenance of Jurassic sandstones on the Norwegian margin, *Geol. Mag.*, 148, 473–480,
954 <https://doi.org/10.1017/S0016756810000877>, 2010.
- 955 Mezger, K., Hanson, G. N., and Bohlen, S. R.: High-precision UPb ages of metamorphic rutile: application to the cooling
956 history of high-grade terranes, *Earth Planet. Sci. Lett.*, 96, 106–118, [https://doi.org/10.1016/0012-821X\(89\)90126-X](https://doi.org/10.1016/0012-821X(89)90126-X), 1989.
- 957 Moecher, D., Hietpas, J., Samson, S., and Chakraborty, S.: Insights into southern Appalachian tectonics from ages of detrital
958 monazite and zircon in modern alluvium, *Geosphere*, 7, 494–512, <https://doi.org/10.1130/GES00615.1>, 2011.
- 959 Möller, A., Mezger, K., and Schenk, V.: U–Pb dating of metamorphic minerals: Pan-African metamorphism and prolonged
960 slow cooling of high pressure granulites in Tanzania, East Africa, *Precambrian Res.*, 104, 123–146,
961 [https://doi.org/10.1016/S0301-9268\(00\)00086-3](https://doi.org/10.1016/S0301-9268(00)00086-3), 2000.
- 962 Morton, A. and Yaxley, G.: Detrital apatite geochemistry and its application in provenance studies, *Geol. Soc. Am. Spec. Pap.*,
963 420, 319–344, [https://doi.org/10.1130/2006.2420\(19\)](https://doi.org/10.1130/2006.2420(19)), 2007.

- 964 Morton, A. C.: Heavy minerals in provenance studies, in: Provenance of Arenites, edited by: Zuffa, G. G., Reidel, Dordrecht,
965 249–277, 1985.
- 966 Mueller, M., Licht, A., Möller, A., Condit, C., Fosdick, J. C., Oçakoğlu, F., and Campbell, C.: Supplemental data for:
967 Navigating the complexity of detrital rutile provenance: Methodological insights from the Neotethys Orogen in Anatolia,
968 <https://doi.org/10.17605/OSF.IO/A4YE5>, 2023.
- 969 Mueller, M. A.: mmueller13/Detrital-UPb-and-TE: v0.2, , <https://doi.org/10.5281/zenodo.10636728>, 2024.
- 970 Mueller, M. A., Licht, A., Campbell, C., Oçakoğlu, F., Taylor, M. H., Burch, L., Ugrai, T., Kaya, M., Kurtoğlu, B., Coster, P.
971 M. C., Métais, G., and Beard, K. C.: Collision Chronology Along the İzmir-Ankara-Erzincan Suture Zone: Insights From the
972 Sarıcakaya Basin, Western Anatolia, *Tectonics*, 38, 3652–3674, <https://doi.org/10.1029/2019TC005683>, 2019.
- 973 Mueller, M. A., Licht, A., Campbell, C., Oçakoğlu, F., Akşit, G. G., Métais, G., Coster, P. M. C., Beard, K. C., and Taylor,
974 M. H.: Sedimentary Provenance From the Evolving Forearc-to-Foreland Central Sakarya Basin, Western Anatolia Reveals
975 Multi-Phase Intercontinental Collision, *Geochem. Geophys. Geosystems*, 23, e2021GC010232,
976 <https://doi.org/10.1029/2021GC010232>, 2022.
- 977 Oçakoğlu, F., Hakyemez, A., Açıkalm, S., Özkan Altıner, S., Büyükmeriç, Y., Licht, A., Demircan, H., Şafak, Ü., Yıldız, A.,
978 Yılmaz, İ. Ö., Wagreich, M., and Campbell, C.: Chronology of subduction and collision along the İzmir-Ankara suture in
979 Western Anatolia: records from the Central Sakarya Basin, *Int. Geol. Rev.*, 1–26,
980 <https://doi.org/10.1080/00206814.2018.1507009>, 2018.
- 981 Odlum, M. L., Stockli, D. F., Capaldi, T. N., Thomson, K. D., Clark, J., Puigdefàbregas, C., and Fildani, A.: Tectonic and
982 sediment provenance evolution of the South Eastern Pyrenean foreland basins during rift margin inversion and orogenic uplift,
983 *Tectonophysics*, 765, 226–248, <https://doi.org/10.1016/j.tecto.2019.05.008>, 2019.
- 984 Odlum, M. L., Capaldi, T. N., Thomson, K. D., and Stockli, D. F.: Tracking cycles of Phanerozoic opening and closing of
985 ocean basins using detrital rutile and zircon geochronology and geochemistry, *Geology*, <https://doi.org/10.1130/G51826.1>,
986 2024.
- 987 Okay, A., Satir, M., and Siebel, W.: Pre-Alpide Palaeozoic and Mesozoic Orogenic Events in the Eastern Mediterranean
988 Region, *Geol. Soc. Lond. Mem.*, 32, 389–405, <https://doi.org/10.1144/GSL.MEM.2006.032.01.23>, 2006.
- 989 Okay, A. I. and Göncüoğlu, M. C.: The Karakaya Complex: A Review of Data and Concepts, *Turk. J. Earth Sci.*, 13, 77–95,
990 2004.
- 991 Okay, A. I. and Kelley, S. P.: Tectonic setting, petrology and geochronology of jadeite + glaucophane and chloritoid +
992 glaucophane schists from north-west Turkey, *J. Metamorph. Geol.*, 12, 455–466, <https://doi.org/10.1111/j.1525-1314.1994.tb00035.x>, 1994.
- 994 Okay, A. I. and Kylander-Clark, A. R. C.: No sediment transport across the Tethys ocean during the latest Cretaceous: detrital
995 zircon record from the Pontides and the Anatolide–Tauride Block, *Int. J. Earth Sci.*, <https://doi.org/10.1007/s00531-022-02275-1>, 2022.
- 997 Okay, A. I., Monod, O., and Monié, P.: Triassic blueschists and eclogites from northwest Turkey: vestiges of the Paleo-Tethyan
998 subduction, *Lithos*, 64, 155–178, [https://doi.org/10.1016/S0024-4937\(02\)00200-1](https://doi.org/10.1016/S0024-4937(02)00200-1), 2002.
- 999 Okay, A. I., Altıner, D., and Kiliç, A. M.: Triassic limestone, turbidites and serpentinite—the Cimmeride orogeny in the Central
1000 Pontides, *Geol. Mag.*, 152, 460–479, <https://doi.org/10.1017/S0016756814000429>, 2015.

- 1001 Okay, A. I., Sunal, G., Sherlock, S., Kylander-Clark, A. R. C., and Özcan, E.: İzmir-Ankara Suture as a Triassic to Cretaceous
1002 Plate Boundary—Data From Central Anatolia, *Tectonics*, 39, e2019TC005849, <https://doi.org/10.1029/2019TC005849>, 2020.
- 1003 Okay, N., Zack, T., Okay, A. I., and Barth, M.: Sinistral transport along the Trans-European Suture Zone: detrital zircon–rutile
1004 geochronology and sandstone petrography from the Carboniferous flysch of the Pontides, *Geol. Mag.*, 148, 380–403,
1005 <https://doi.org/10.1017/S0016756810000804>, 2011.
- 1006 O’Sullivan, G., Chew, D., Kenny, G., Henrichs, I., and Mulligan, D.: The trace element composition of apatite and its
1007 application to detrital provenance studies, *Earth-Sci. Rev.*, 201, 103044, <https://doi.org/10.1016/j.earscirev.2019.103044>,
1008 2020.
- 1009 O’Sullivan, G. J., Chew, D. M., and Samson, S. D.: Detecting magma-poor orogens in the detrital record, *Geology*, 44, 871–
1010 874, <https://doi.org/10.1130/G38245.1>, 2016.
- 1011 Paterson, S. R. and Ducea, M. N.: Arc Magmatic Tempos: Gathering the Evidence, *Elements*, 11, 91–98,
1012 <https://doi.org/10.2113/gselements.11.2.91>, 2015.
- 1013 Paton, C., Hellstrom, J., Paul, B., Woodhead, J., and Hergt, J.: Iolite: Freeware for the visualisation and processing of mass
1014 spectrometric data, *J. Anal. At. Spectrom.*, 26, 2508, <https://doi.org/10.1039/c1ja10172b>, 2011.
- 1015 Pereira, I. and Storey, C. D.: Detrital rutile: Records of the deep crust, ores and fluids, *Lithos*, 107010,
1016 <https://doi.org/10.1016/j.lithos.2022.107010>, 2023.
- 1017 Pereira, I., Storey, C. D., Strachan, R. A., Bento dos Santos, T., and Darling, J. R.: Detrital rutile ages can deduce the tectonic
1018 setting of sedimentary basins, *Earth Planet. Sci. Lett.*, 537, 116193, <https://doi.org/10.1016/j.epsl.2020.116193>, 2020.
- 1019 Pereira, I., Storey, C. D., Darling, J. R., Moreira, H., Strachan, R. A., and Cawood, P. A.: Detrital rutile tracks the first
1020 appearance of subduction zone low T/P paired metamorphism in the Palaeoproterozoic, *Earth Planet. Sci. Lett.*, 570, 117069,
1021 <https://doi.org/10.1016/j.epsl.2021.117069>, 2021.
- 1022 Pickett, E. A. and Robertson, A. H. F.: Formation of the Late Palaeozoic–Early Mesozoic Karakaya Complex and related
1023 ophiolites in NW Turkey by Palaeotethyan subduction–accretion, *J. Geol. Soc.*, 153, 995–1009,
1024 <https://doi.org/10.1144/gsjgs.153.6.0995>, 1996.
- 1025 Plavsa, D., Reddy, S. M., Agangi, A., Clark, C., Kylander-Clark, A., and Tiddy, C. J.: Microstructural, trace element and
1026 geochronological characterization of TiO₂ polymorphs and implications for mineral exploration, *Chem. Geol.*, 476, 130–149,
1027 <https://doi.org/10.1016/j.chemgeo.2017.11.011>, 2018.
- 1028 Poulaki, E. M., Stockli, D. F., and Shuck, B. D.: Pre-Subduction Architecture Controls Coherent Underplating During
1029 Subduction and Exhumation (Nevado-Filábride Complex, Southern Spain), *Geochem. Geophys. Geosystems*, 24,
1030 e2022GC010802, <https://doi.org/10.1029/2022GC010802>, 2023.
- 1031 Pourteau, A., Oberhänsli, R., Candan, O., Barrier, E., and Vrielynck, B.: Neotethyan closure history of western Anatolia: a
1032 geodynamic discussion, *Int. J. Earth Sci.*, 105, 203–224, <https://doi.org/10.1007/s00531-015-1226-7>, 2016.
- 1033 Rösel, D., Boger, S. D., Möller, A., Gaitzsch, B., Barth, M., Oalman, J., and Zack, T.: Indo-Antarctic derived detritus on the
1034 northern margin of Gondwana: evidence for continental-scale sediment transport, *Terra Nova*, 26, 64–71,
1035 <https://doi.org/10.1111/ter.12070>, 2014.

- 1036 Rösel, D., Zack, T., and Möller, A.: Interpretation and significance of combined trace element and U–Pb isotopic data of
1037 detrital rutile: a case study from late Ordovician sedimentary rocks of Saxo-Thuringia, Germany, *Int. J. Earth Sci.*, 108, 1–25,
1038 <https://doi.org/10.1007/s00531-018-1643-5>, 2019.
- 1039 Rudnick, R., Barth, M., Horn, I., and McDonough, W. F.: Rutile-Bearing Refractory Eclogites: Missing Link Between
1040 Continents and Depleted Mantle, *Science*, 287, 278–281, <https://doi.org/10.1126/science.287.5451.278>, 2000.
- 1041 Schärer, U., Krogh, T. E., and Gower, C. F.: Age and evolution of the Grenville Province in eastern Labrador from U–Pb
1042 systematics in accessory minerals, *Contrib. Mineral. Petrol.*, 94, 438–451, <https://doi.org/10.1007/BF00376337>, 1986.
- 1043 Schmitz, M. D. and Bowring, S. A.: Constraints on the thermal evolution of continental lithosphere from U–Pb accessory
1044 mineral thermochronometry of lower crustal xenoliths, southern Africa, *Contrib. Mineral. Petrol.*, 144, 592–618,
1045 <https://doi.org/10.1007/s00410-002-0419-9>, 2003.
- 1046 Schoene, B.: U–Th–Pb Geochronology, in: *Treatise on Geochemistry*, Elsevier, 341–378, <https://doi.org/10.1016/B978-0-08-095975-7.00310-7>, 2014.
- 1048 Şengör, A. M. C. and Yilmaz, Y.: Tethyan evolution of turkey: a plate tectonic approach, *Tectonophysics*, 75, 181–241, 1981.
- 1049 Şengör, A. M. C., Yilmaz, Y., and Sungurlu, O.: Tectonics of the Mediterranean Cimmerides: nature and evolution of the
1050 western termination of Palaeo-Tethys, *Geol. Soc. Lond. Spec. Publ.*, 17, 77–112,
1051 <https://doi.org/10.1144/GSL.SP.1984.017.01.04>, 1984.
- 1052 Şengün, F., Zack, T., and Dunkl, I.: Provenance of detrital rutiles from the Jurassic sandstones in the Central Sakarya Zone,
1053 NW Turkey: U–Pb ages and trace element geochemistry, *Geochemistry*, 80, 125667,
1054 <https://doi.org/10.1016/j.chemer.2020.125667>, 2020.
- 1055 Shaanan, U., Avigad, D., Morag, N., Güngör, T., and Gerdes, A.: Drainage response to Arabia–Eurasia collision: Insights from
1056 provenance examination of the Cyprian Kythrea flysch (Eastern Mediterranean Basin), *Basin Res.*, n/a,
1057 <https://doi.org/10.1111/bre.12452>, 2020.
- 1058 Sharman, G. R., Sharman, J. P., and Sylvester, Z.: detritalPy: A Python-based toolset for visualizing and analysing detrital
1059 geo-thermochronologic data, *Depositional Rec.*, 4, 202–215, <https://doi.org/10.1002/dep2.45>, 2018.
- 1060 Sherlock, S., Kelley, S., Inger, S., Harris, N., and Okay, A.: ⁴⁰Ar–³⁹Ar and Rb–Sr geochronology of high-pressure
1061 metamorphism and exhumation history of the Tavsanli Zone, NW Turkey, *Contrib. Mineral. Petrol.*, 137, 46–58,
1062 <https://doi.org/10.1007/PL00013777>, 1999.
- 1063 Simonetti, A., Heaman, L. M., Hartlaub, R. P., Creaser, R. A., MacHattie, T. G., and Böhm, C.: U–Pb zircon dating by laser
1064 ablation-MC-ICP-MS using a new multiple ion counting Faraday collector array, *J. Anal. At. Spectrom.*, 20, 677–686,
1065 <https://doi.org/10.1039/B504465K>, 2005.
- 1066 Smye, A. J. and Stockli, D. F.: Rutile U–Pb age depth profiling: A continuous record of lithospheric thermal evolution, *Earth
1067 Planet. Sci. Lett.*, 408, 171–182, <https://doi.org/10.1016/j.epsl.2014.10.013>, 2014.
- 1068 Smye, A. J., Marsh, J. H., Vermeesch, P., Garber, J. M., and Stockli, D. F.: Applications and limitations of U–Pb
1069 thermochronology to middle and lower crustal thermal histories, *Chem. Geol.*, 494, 1–18,
1070 <https://doi.org/10.1016/j.chemgeo.2018.07.003>, 2018.

- 1071 Stacey, J. S. and Kramers, J. D.: Approximation of terrestrial lead isotope evolution by a two-stage model, *Earth Planet. Sci. Lett.*, 26, 207–221, [https://doi.org/10.1016/0012-821X\(75\)90088-6](https://doi.org/10.1016/0012-821X(75)90088-6), 1975.
1072
- 1073 Steiger, R. H. and Jäger, E.: Subcommittee on geochronology: Convention on the use of decay constants in geo- and
1074 cosmochronology, *Earth Planet. Sci. Lett.*, 36, 359–362, [https://doi.org/10.1016/0012-821X\(77\)90060-7](https://doi.org/10.1016/0012-821X(77)90060-7), 1977.
- 1075 Storey, C. D., Jeffries, T. E., and Smith, M.: Common lead-corrected laser ablation ICP–MS U–Pb systematics and
1076 geochronology of titanite, *Chem. Geol.*, 227, 37–52, <https://doi.org/10.1016/j.chemgeo.2005.09.003>, 2006.
- 1077 Storey, C. D., Smith, M. P., and Jeffries, T. E.: In situ LA-ICP-MS U–Pb dating of metavolcanics of Norrbotten, Sweden:
1078 Records of extended geological histories in complex titanite grains, *Chem. Geol.*, 240, 163–181,
1079 <https://doi.org/10.1016/j.chemgeo.2007.02.004>, 2007.
- 1080 Sundell, K. E., George, S. W. M., Carrapa, B., Gehrels, G. E., Ducea, M. N., Saylor, J. E., and Pepper, M.: Crustal Thickening
1081 of the Northern Central Andean Plateau Inferred From Trace Elements in Zircon, *Geophys. Res. Lett.*, 49, e2021GL096443,
1082 <https://doi.org/10.1029/2021GL096443>, 2022.
- 1083 Tang, M., Ji, W.-Q., Chu, X., Wu, A., and Chen, C.: Reconstructing crustal thickness evolution from europium anomalies in
1084 detrital zircons, *Geology*, 49, 76–80, <https://doi.org/10.1130/G47745.1>, 2020.
- 1085 Templ, M., Hron, K., and Filzmoser, P.: robCompositions: An R-package for Robust Statistical Analysis of Compositional
1086 Data, in: *Compositional Data Analysis*, John Wiley & Sons, Ltd, 341–355, <https://doi.org/10.1002/9781119976462.ch25>,
1087 2011.
- 1088 Tera, F. and Wasserburg, G. J.: U-Th-Pb systematics in three Apollo 14 basalts and the problem of initial Pb in lunar rocks,
1089 *Earth Planet. Sci. Lett.*, 14, 281–304, [https://doi.org/10.1016/0012-821X\(72\)90128-8](https://doi.org/10.1016/0012-821X(72)90128-8), 1972.
- 1090 Tomkins, H. S., Powell, R., and Ellis, D. J.: The pressure dependence of the zirconium-in-rutile thermometer, *J. Metamorph.*
1091 *Geol.*, 25, 703–713, <https://doi.org/10.1111/j.1525-1314.2007.00724.x>, 2007.
- 1092 Topuz, G., Altherr, R., Schwarz, W. H., Dokuz, A., and Meyer, H.-P.: Variscan amphibolite-facies rocks from the Kurtoğlu
1093 metamorphic complex (Gümüşhane area, Eastern Pontides, Turkey), *Int. J. Earth Sci.*, 96, 861–873,
1094 <https://doi.org/10.1007/s00531-006-0138-y>, 2007.
- 1095 Topuz, G., Candan, O., Okay, A. I., von Quadt, A., Othman, M., Zack, T., and Wang, J.: Silurian anorogenic basic and acidic
1096 magmatism in Northwest Turkey: Implications for the opening of the Paleo-Tethys, *Lithos*, 356–357, 105302,
1097 <https://doi.org/10.1016/j.lithos.2019.105302>, 2020.
- 1098 Triebold, S., von Eynatten, H., Luvizotto, G. L., and Zack, T.: Deducing source rock lithology from detrital rutile geochemistry:
1099 An example from the Erzgebirge, Germany, *Chem. Geol.*, 244, 421–436, <https://doi.org/10.1016/j.chemgeo.2007.06.033>,
1100 2007.
- 1101 Triebold, S., Luvizotto, G. L., Tolosana-Delgado, R., Zack, T., and von Eynatten, H.: Discrimination of TiO₂ polymorphs in
1102 sedimentary and metamorphic rocks, *Contrib. Mineral. Petrol.*, 161, 581–596, <https://doi.org/10.1007/s00410-010-0551-x>,
1103 2011.
- 1104 Triebold, S., von Eynatten, H., and Zack, T.: A recipe for the use of rutile in sedimentary provenance analysis, *Sediment.*
1105 *Geol.*, 282, 268–275, <https://doi.org/10.1016/j.sedgeo.2012.09.008>, 2012.

- 1106 Ustaömer, P., Ustaömer, T., and Robertson, Alastair. H. F.: Ion Probe U-Pb Dating of the Central Sakarya Basement: A peri-
1107 Gondwana Terrane Intruded by Late Lower Carboniferous Subduction/Collision-related Granitic Rocks, *Turk. J. Earth Sci.*,
1108 21, 905–932, <https://doi.org/10.3906/yer-1103-1>, 2012.
- 1109 Ustaömer, T., Robertson, A. H. F., Ustaömer, P. A., Gerdes, A., and Peytcheva, I.: Constraints on Variscan and Cimmerian
1110 magmatism and metamorphism in the Pontides (Yusufeli–Artvin area), NE Turkey from U–Pb dating and granite
1111 geochemistry, *Geol. Soc. Lond. Spec. Publ.*, 372, 49–74, <https://doi.org/10.1144/SP372.13>, 2013.
- 1112 Ustaömer, T., Ustaömer, P., Robertson, A. H. F., and Gerdes, A.: Implications of U–Pb and Lu–Hf isotopic analysis of detrital
1113 zircons for the depositional age, provenance and tectonic setting of the Permian–Triassic Palaeotethyan Karakaya Complex,
1114 NW Turkey, *Int. J. Earth Sci.*, 105, 7–38, <https://doi.org/10.1007/s00531-015-1225-8>, 2016.
- 1115 Vermeesch, P.: Unifying the U–Pb and Th–Pb methods: joint isochron regression and common Pb correction, *Geochronology*,
1116 2, 119–131, <https://doi.org/10.5194/gchron-2-119-2020>, 2020.
- 1117 Vermeesch, P.: On the treatment of discordant detrital zircon U–Pb data, *Geochronology*, 3, 247–257,
1118 <https://doi.org/10.5194/gchron-3-247-2021>, 2021.
- 1119 Vry, J. K. and Baker, J. A.: LA-MC-ICPMS Pb–Pb dating of rutile from slowly cooled granulites: Confirmation of the high
1120 closure temperature for Pb diffusion in rutile, *Geochim. Cosmochim. Acta*, 70, 1807–1820,
1121 <https://doi.org/10.1016/j.gca.2005.12.006>, 2006.
- 1122 Watson, E. B., Wark, D. A., and Thomas, J. B.: Crystallization thermometers for zircon and rutile, *Contrib. Mineral. Petrol.*,
1123 151, 413, <https://doi.org/10.1007/s00410-006-0068-5>, 2006.
- 1124 Williams, I. S.: U-Th-Pb Geochronology by Ion Microprobe, in: Applications of Microanalytical Techniques to Understanding
1125 Mineralizing Processes, Society of Economic Geologists, 1–35, <https://doi.org/10.5382/Rev.07.01>, 1997.
- 1126 Xiong, X. L., Adam, J., and Green, T. H.: Rutile stability and rutile/melt HFSE partitioning during partial melting of hydrous
1127 basalt: Implications for TTG genesis, *Chem. Geol.*, 218, 339–359, <https://doi.org/10.1016/j.chemgeo.2005.01.014>, 2005.
- 1128 Yildiz, A., Kibici, Y., Bağcı, M., Dumlupınar, İ., Kocabaş, C., and Aritan, A. E.: Petrogenesis of the post-collisional Eocene
1129 volcanic rocks from the Central Sakarya Zone (Northwestern Anatolia, Turkey): Implications for source characteristics,
1130 magma evolution, and tectonic setting, *Arab. J. Geosci.*, 8, 11239–11260, <https://doi.org/10.1007/s12517-015-1991-4>, 2015.
- 1131 Zack, T. and Kooijman, E.: Petrochronology and Geochronology of Rutile, *Rev. Mineral. Geochem.*, 83, 443–467, 2017.
- 1132 Zack, T., von Eynatten, H., and Kronz, A.: Rutile geochemistry and its potential use in quantitative provenance studies,
1133 *Sediment. Geol.*, 171, 37–58, <https://doi.org/10.1016/j.sedgeo.2004.05.009>, 2004a.
- 1134 Zack, T., Moraes, R., and Kronz, A.: Temperature dependence of Zr in rutile: empirical calibration of a rutile thermometer,
1135 *Contrib. Mineral. Petrol.*, 148, 471–488, <https://doi.org/10.1007/s00410-004-0617-8>, 2004b.
- 1136 Zack, T., Stockli, D. F., Luvizotto, G. L., Barth, M. G., Belousova, E., Wolfe, M. R., and Hinton, R. W.: In situ U–Pb rutile
1137 dating by LA-ICP-MS: 208Pb correction and prospects for geological applications, *Contrib. Mineral. Petrol.*, 162, 515–530,
1138 <https://doi.org/10.1007/s00410-011-0609-4>, 2011.
- 1139 Zoleikhaei, Y., Mulder, J. A., and Cawood, P. A.: Integrated detrital rutile and zircon provenance reveals multiple sources for
1140 Cambrian sandstones in North Gondwana, *Earth-Sci. Rev.*, 213, 103462, <https://doi.org/10.1016/j.earscirev.2020.103462>,
1141 2021.

